TOPOLOGY OF EQUATORIAL TIMELIKE CIRCULAR ORBITS AROUND KERR-LIKE BLACK HOLES

By

Fatima Arshad

NATIONAL UNIVERSITY OF MODERN LANGUAGES
ISLAMABAD

December, 2024

TOPOLOGY OF EQUATORIAL TIMELIKE CIRCULAR ORBITS AROUND KERR-LIKE BLACK HOLES

By

Fatima Arshad

MS-Math, National University of Modern Languages, Islamabad, 2024

A THESIS SUBMITTED IN PARTIAL FULFILMENT OF
THE REQUIREMENTS FOR THE DEGREE OF

MASTER OF SCIENCE
In **Mathematics**

To
FACULTY OF ENGINEERING & COMPUTING

NATIONAL UNIVERSITY OF MODERN LANGUAGES ISLAMABAD

NATIONAL UNIUVERSITY OF MODERN LANGUAGES

FACULTY OF ENGINEERIING & COMPUTER SCIENCE

THESIS AND DEFENSE APPROVAL FORM

The undersigned certify that they have read the following thesis, examined the defense, are satisfied with overall exam performance, and recommend the thesis to the Faculty of Engineering and Computing for acceptance.

Thesis Title: Topology of Equatorial Timelike Circular Orbits Around Kerr-like Black Holes.

Submitted By: Fatima Arshad **Registration #:**70 MS/MATH/F22

Master of Science in Mathematics

Title of the Degree

Mathematics

Name of Discipline

Dr. Muhammad Rizwan	
Name of Research Supervisor	Signature of Research Supervisor
Dr. Sadia Riaz	
Name of HOD (MATH)	Signature of HOD (MATH)
Dr. Noman Malik	
Name of Dean (FEC)	Signature of Dean (FEC)

December 06, 2024

AUTHOR’S DECLARATION

I am Fatima Arshad
Daughter of Arshad Iqbal
Discipline Mathematics

Candidate of Master of Science in Mathematics at the National University of Modern Languages do hereby declare that the thesis Topology of Equatorial Timelike Circular Orbits Around Kerr-like Black Holes submitted by me in partial fulfillment of MS degree, is my original work and has not been submitted or published earlier. I also solemnly declare that it shall not, in the future, be submitted by me for obtaining any other degree from this or any other university or institution. I also understand that if evidence of plagiarism is found in my thesis/dissertation at any stage, even after the award of a degree, the work may be canceled and the degree revoked.

Signature of Candidate

Fatima Arshad
Name of Candidate

December 06, 2024
Date

ABSTRACT

Title: Topology of Equatorial Timelike Circular Orbits Around Kerr-like Black Holes

A topological approach has been successfully used to study the properties of the light ring and null circular orbit in generic black hole spacetime. In this work, a detailed review of the general framework is extended to investigate the topology of equatorial timelike circular orbits (TCOs) around a generic asymmetric, stationary, asymptotically flat black hole spacetime. The topological analysis of the Kerr black hole and Kerr-like black holes in a perfect fluid dark matter (PFDM) background is conducted. It is found that the dynamics of test particles affected by the gravitational field of the black hole are examined using a unique topological framework developed for generic axisymmetric stationary, asymptotically flat black holes. Furthermore, when the angular momentum is held constant, there are two possibilities: 1) the absence of timelike circular orbits, or 2) the presence of TCOs occurring in pairs, with one stable and one unstable. Additionally, the stable and unstable timelike circular orbits have positive and negative winding numbers, respectively, and the radii of these circular orbits correspond to the zero points of the constructed n vector field. Similar results are observed for black holes in a PFDM background. However, for any fixed value of the particle parameter, the presence of PFDM increases the radius of TCOs.

TABLE OF CONTENTS

LIST OF FIGURES

LIST OF ABBREVIATIONS

BH	-	Black Hole
EFE	-	Einstein Field Equations
ISCO	-	Innermost stable circular orbit
MSCO	-	Marginally stable circular orbit
LR	-	Light Ring
PFDM	-	Perfect Fluid Dark Matter
TCOs		Timelike Circular Orbits

LIST OF SYMBOLS

M - Mass

G - Gravitational constant

F - Force

r - Distance

c - Speed of light

v - Speed of object

l - Angular momentum

Q - electric charge

E - Energy

ACKNOWLEDGMENT

Firstly, I wish to express my deep gratitude and appreciation to Almighty Allah, who made this study possible and successful. This work would not have been accomplished without the genuine support from various sources, for which I am sincerely thankful. There were many significant contributors to my success, and I must particularly acknowledge my research supervisor, Dr. Muhammad Rizwan, who provided unwavering guidance throughout my research journey. I sincerely appreciate our Head of Department, Dr. Sadia Riaz, for providing us with a supportive research environment and for her kind assistance. I would also like to extend my heartfelt thanks to our esteemed teachers, Dr. Kamran Qadir, Dr. Anum Naseem, Dr. Hadia Tariq, Dr. Afshan Qayyum and others, for their guidance and support.

I would also like to acknowledge the invaluable support from the administration of the Department of Mathematics, who assisted me throughout my research and helped to simplify the challenges I encountered. To all those I haven’t mentioned but whose contributions were significant, I extend my heartfelt thanks.

DEDICATION

I dedicate my thesis to my parents and teachers for their endless support and encouragement throughout my pursuit of education, I hope this achievement will fulfill the dream they envisioned for me.

CHAPTER 1

INTRODUCTION

1.1 General Relativity

In Newton's theory of gravity, time is regarded as an absolute quantity, that is the same for everyone, regardless of whether the observer is moving or stationary or whether the observer is close to or far from a gravitational object. Newton's in his theory of gravitation considered, the arena of physics as a 3-dimensional space. Additionally, he considered gravity an attractive force between objects, directly proportional to the product of their masses and inversely proportional to the square of the distance between them. This relationship can be expressed mathematically as follows:

$$F = G\frac{m_1 m_2}{r^2}, \tag{1.1}$$

where m_1, m_2 represent the masses of the objects and $G = 6.674 \times 10^{-11} Nm^2 kg^{-2}$ is a universal gravitational constant. Newton provides the formula for gravitational force between objects, but he did not explain the source of this force, such as how objects far apart can attract each other. Newtonian mechanics work very effectively for objects moving at slow speeds and in weak gravity regimes. Newton's law of gravity is considered a law rather than a theory since it specifies the force of gravity without going into the principles that explain it. The law of gravity applies to all objects with mass in the universe. It controls the motion of heavenly bodies such as planets, stars, and moons, as well as ordinary objects on Earth. While highly effective for many practical purposes. However, this theory has significant limitations. It can not precisely account for the precession of Mercury's orbit, relies on the problematic notion of instantaneous gravitational effects, fails to fully incorporate the mathematical concept of similarity, (the indistinguishable of gravitational and inertial weight), and diverges from observed behaviours under very strong gravitational fields or at velocities approaching the speed of light.

In Einstein's theory of gravitation, he suggested that time is not a universal quantity; it depends on the observer's velocity and location. An observer moving at a velocity close to the speed of light experiences a significant difference in time compared to an observer at rest. Similarly, an observer close to a strong gravitational object or field experiences a significant difference in time compared to an observer far away from the gravitational object. Thus, in his theory, Einstein considered 1-dimension of time and 3-dimensions of space, defining the new concept of a single 4-dimensional continuum called spacetime. J. A Wheeler [1] defines spacetime as "the arena of physics," which includes all events that occur at certain times and locations in space. Mathematically, spacetime is a 4-dimensional manifold (M,g) that locally resembles 4-dimensional Euclidean space, but globally it can be curved depending on the mass distribution within it. The metric tensor $g_{\mu\nu}$ is used to represent spacetime geometric properties and to define physical quantities and laws in it. Further, Einstein suggested that gravity is not a force like other forces; rather, it arises as a consequence of spacetime curvature due to the distribution of mass and energy. The distribution of mass (or energy), such as that of the Sun, causes spacetime to curve. As a result, other bodies, such as Earth, do not move in their orbits due to gravitational attraction, but instead follow the straightest possible (available) path through the curved spacetime. J.A. Wheeler summarizes gravity as; *"Space acts on matter, telling how to move. In turn, matter reacts back on space, telling it how to curve"* [1].

In 1915, Einstein presented his theory of gravitation which relates spacetime geometry to the distribution of mass and energy through the Einstein field equations (EFEs), defined as: [1, 2]

$$R_{\mu\nu} - \frac{1}{2}g_{\mu\nu}R + \Lambda g_{\mu\nu} = \frac{8\pi G}{c^4}T_{\mu\nu}, \tag{1.2}$$

where G is the gravitational constant, c is the speed of light, Λ is the cosmological constant, $R_{\mu\nu}$ is the Ricci tensor, R is the Ricci scalar, and $T_{\mu\nu}$ is the energy-momentum tensor. He included the cosmological constant Λ in field equations to model the Universe's static nature. However, in 1929, Edwin Hubble discovered that our Universe is expanding [3]. So, He excluded the Λ term from EFEs and called the inclusion of this term the biggest blunder of his life. The recent scientific data predicted that our Universe's expansion is speeding [4]. This raises the idea of a vacuum energy, sometimes known as dark energy. Later, a positive value of Λ is introduced to define the Universe's acceleration, and the Λ term is considered as part of the energy-stress tensor. Thus, the EFEs can be expressed as:

$$R_{\mu\nu}-\frac{1}{2}g_{\mu\nu}R=\frac{8\pi G}{c^4}T_{\mu\nu}. \tag{1.3}$$

The left side of the equation represents spacetime geometry, whereas the right side represents energy or matter distribution. Note that, here Ricci tensor $R_{\mu\nu}$ and energy-momentum tensor $T_{\mu\nu}$ are symmetric tensors so, on changing the indices reduces the EFEs to ten non-linear second-order coupled partial differential equations in ten functions $(g_{\mu\nu})$ and ten functions $(T_{\mu\nu})$ of four independent variables (x^{μ}). Solving EFEs with a generalized metric is challenging because they are coupled non-linear differential equations.

So, instead of obtaining a generic solution, we focus on physically relevant energy-momentum tensors and make assumptions regarding spacetime symmetry. These assumptions reduce the number of unknown functions $(g_{\mu\nu})$ that can be effectively determined. Furthermore, the equations can be simplified by selecting an appropriate energy-momentum tensor. Here are some physically relevant energy-momentum tensors:

The energy-momentum tensor of the electromagnetic field is defined as

$$T_{\mu\nu}=F_{\mu\delta}F^{\delta}_{\nu}-\frac{1}{4}g_{\mu\nu}F_{\delta\lambda}F^{\delta\lambda}, \tag{1.4}$$

where $F_{\mu\nu}$ is a skew-symmetric electromagnetic tensor, defined as

$$F_{\mu\nu}=\partial_{\mu}A_{\nu}-\partial_{\nu}A_{\mu}, \tag{1.5}$$

$A_{\mu}=(-\phi,\underline{A})$ with a 4-electromagnetic potential. The remaining frame mass density ρ and the isotropic pressure p can be used to characterize the tensor of energy-momentum for the perfect fluid, which is represented as

$$T_{\mu\nu}=(\rho+p)u_{\mu}u_{\nu}-pg_{\mu\nu}, \tag{1.6}$$

where u_{μ} indicates components of the fluid velocity. The simplest example is a vacuum with no matter $(T_{\mu\nu}=0)$ everywhere.

The Minkowski spacetime of special relativity is characterized by maximum symmetry and a vacuum situation, that is, $(T_{\mu\nu}=0)$. The line element (or interval) between the two o in this space can be expressed as

$$ds^2=-c^2dt^2+dx^2+dy^2+dz^2. \tag{1.7}$$

The Minkowski metric is a trivial solution to EFEs [1].

1.2 Black Hole

A gravitational body's escape velocity at a point in its gravitational field is defined as the minimum velocity required for any (test) object to escape the body's gravitational field. The escape velocity, v_{esc}, at every point P at the distance r from the gravitational body's mass center can be calculated using the following formula if M is the body's mass.

$$\text{Kinetic Energy} + \text{Gravitational Potential Energy} = 0. \tag{1.8}$$

The Kinetic energy (K.E) is the energy associated with an object's motion and may be calculated using the formula $K.E = mv^2$, where "v" is the speed of the objects. Gravitational potential energy (P.E) is an energy due to position. At the distance r from the mass center of the gravitational body, it is given as $P.E = -GMm/r$. Thus, for the escape velocity we have

$$\frac{1}{2}mv_{\text{esc}}^2 = \frac{GMm}{r}. \tag{1.9}$$

Here the left-hand side of the above equation represents the kinetic energy and the right-hand side represents the negative potential energy. Thus, the expression for the escape velocity of the gravitational body can be obtained from the above equation which yields the result as [5].

$$v_{\text{esc}} = \sqrt{\frac{2GM}{r}}. \tag{1.10}$$

This result shows that the escape velocity of any gravitational body at some point in its gravitational field depends only on its mass M and the distance r from the body's center of mass, but not on the mass of the test object. Thus, we can say that the escape velocity of the gravitational body is the same as that of a tiny test object and as well as massive test object. Furthermore, at each location in the gravitational field, The gravitational body's mass M squared determines the escape velocity v_{esc}, which is inversely associated with the product of the square root of the distance r from the center of mass. For reference, the escape velocity of Earth ($M = 6 \times 10^24$ kg) at its surface ($r = 6400$ km) is (approximately) 11.186 km/s, while that of the Sun ($M = 1.9891 \times 10^{30}$ kg) at its surface ($r = 1.4 \times 10^6$ km) is 617.5 km/s. So, if we fire any test object of any mass from the surface of Earth with an initial velocity of 11.186 km/s, it will not return but escape Earth's gravitational field. Note that, if altitude is gained from the surface of Earth and fire the same object again, then it require less initial velocity to escape from the gravitational field. This is because increasing r which will decrease the value of escape velocity.

In a letter to Henry Cavendish in 1784, John Michell proposed that dark stars with sufficient mass and density might have an escape velocity at the surface greater than the speed of light, resulting in the absence of light. Although these dark stars cannot be observed, they can be recognized by their strong gravitational attraction on nearby objects [6]. In 1796, Marquis de Laplace proposed the same idea in his book "The System of the World" [7, 8]. The above-mentioned proposals for the existence of dark stars are based on the theory that light is composed of particles and, therefore, can be attracted by gravity just like any other particle. Later on, it was proposed that light is made up of waves, so there was no explanation for the bending of light due to gravity. Therefore, at that period, the concept of dark stars remained neglected until Einstein presented his general relativity theory. Gravity is defined by Einstein's general theory of relativity as a spacetime curvature that can change light's course. In 1916, Karl Schwarzschild proposed the first EFE solution, reopening the issue of the dark star, which was eventually termed BH in 1969 by J. A. Wheeler [9].

Astrophysically, A black hole is considered to be the final stage/outcome in the gravitational collapse of a large star. Initially, it was assumed that the BH solution of EFEs had no astrophysical significance. In the 1920s, it was discovered that when a big star reaches the end of its life cycle, the degenerate pressure of electrons prevents it from collapsing without nuclear fusion, leading to its death as a white dwarf. In 1931, Subrahmanyam Chandrasekhar proposed that if a star's mass exceeds the Chandrasekhar limit (about 1.44 times the solar mass), degenerate electron pressure is insufficient to avoid gravitational collapse [10]. Most scientists, including Arthur Eddington, rejected his proposal. They believed in the existence of a mechanism capable of avoiding total collapse [11].

It was discovered that if a star's mass is greater than the Chandrasekhar limit, its collapse to a point can be stopped by degenerate neutron pressure, resulting in the formation of a neutron star [12]. In 1939, Albert Einstein argued that stars can't shrink to zero size or for heavenly objects have so intense gravity that light cannot escape from their surfaces [13]. In the same year that Einstein rejected the existence of the BH, J. R. Oppenheimer and H. S. Snyder wrote an essay on gravitational collapse, discussing how a BH can originate from gravitation collapse [14]. However, the telescopes of the time were unable to discover any observable results. This conclusion reopened the discussion over the existence of the BH.

The Quasars, or highly active galactic nuclei, were found in the 1950s. Initially, the process causing these quasars was unknown. In 1964, Edwin Salpeter and Yakov Zel'dovich first postulated that quasars could black holes are powered by material dragged from surrounding massive stars, known as accretion disks [15, 16]. In 1964, the Cygnus X-1 was discovered and identified as the first BH [17]. In 1971, it was discovered that Cygnus X-1 had a large star companion. Furthermore, researching its orbital motion revealed that its mass is greater than that of the neutron star, leading to the conclusion that it is a stellar mass BH. This convinces researchers in this field to believe in the presence of BH in our universe. Recent technological advancements have enabled the identification of the LIGO/Virgo merger of two black holes resulted in gravitational waves, leading to new paths in BH astrophysics [18, 19]. In 2019, astronomers used the EHT (Event Horizon Telescope) to obtain the first picture of a massive BH (6.5 billion times the solar mass) in the galaxy's center $M87$ [20]. These discoveries confirm the existence of black holes, as proposed by Newton and Einstein's gravity theories. They also provide an original viewpoint on the subject. Researchers will explore many elements of the black hole.

A black hole is a massive gravitational object with so strong gravity that its escape velocity is greater than the speed of light [1, 5]. Nothing, not even light, can escape the black hole's gravitational pull since its escape velocity is higher than the velocity of light. There exists a surface in the spacetime of BHs where the escape velocity equals the speed of light $(v_{esc} = c)$. While the escape velocity outside the surface is smaller $(v_{esc} < c)$, it is greater inside the surface $(v_{esc} > c)$. The above equation demonstrates that the location of this surface can be found by substituting $v_{esc} = c$.

$$r_s = \frac{2GM}{c^2}. \tag{1.11}$$

The black hole considers this surface to be its event horizon. The light inside this surface loses its ability to escape, hence it is frequently called the boundary of the BHs. Events within the black hole's horizon have no impact on the outside world. The event horizon is a null hypersurface in 4-dimensional BH spacetime, defined as any vector (v_1) with components. A^1 vector at a point p in spacetime assigns a real number $v(f)$ to each differentiable function f defined on spacetime. On this surface, v^α is a null vector $(v^\mu v_\mu = 0)$. Light emitted at this surface remains on the surface.

1.2.1 Static and Stationary Black Hole

A spacetime is considered stationary if it has a time-like Killing vector (∂t). This indicates that the metric components $g_{\mu\nu}$ are independent on t, and $\partial g_{\mu\nu}/\partial t = 0$. A stationary spacetime is static if its line element remains constant as the time coordinate changes from $t \to -t$. A spacetime is axisymmetric if its metric components don't depend on the coordinate ϕ, the azimuthal angle with concern to the symmetry axis, that is, $\partial g_{\mu\nu}/\partial\phi = 0$, and remain invariant upon the replacement of $\phi \to -\phi$. To satisfy the following constraints, the spacetime must be stationary and axisymmetric, with all metric components independent of t and ϕ and $g_{tr} = g_{r\phi} = g_{t\phi} = g_{t\phi} = 0$.

1.2.2 Schwarzschild Black Hole

To find a solution, he examined the space-time vacuum around a spherically symmetric mass M located at the origin. The Schwarzschild metric is a just approximation of the field of gravity outside of spherical symmetric nonrotating sources like stars, planets, or static black holes BHs. Mathematically, the Schwarzschild line element in spherical coordinates can be represented as [1, 2].

$$ds^2 = -\left(1 - \frac{2GM}{c^2 r}\right)(cdt)^2 + \left(1 - \frac{2GM}{c^2 r}\right)^{-1} dr^2 + r^2 d\theta^2 + r^2 \sin^2\theta d\phi^2, \tag{1.12}$$

where M is the mass of the gravitational source. In natural units $(G = 1 = c)$, the line element of the Schwarzschild BH can be expressed as

$$ds^2 = -\left(1 - \frac{2GM}{c^2 r}\right)(cdt)^2 + \left(1 - \frac{2GM}{c^2 r}\right)^{-1} dr^2 + r^2 d\theta^2 + r^2 \sin^2\theta d\phi^2. \tag{1.13}$$

The metric components at $r = 2M$ and $r = 0$, $g_{\mu\nu}$ showed unusual behaviour, as shown in the equation above. The metric and spacetime are no longer well-defined when $r = 0$, as both metric components at $r = 2M, g_{tt} = 0$, and g_{rr} is infinite. The point $r = 0$ in the Schwarzschild spacetime represents a critical (crushing) singularity, where the spacetime curvature becomes infinite, and the principles of physics break down. The coordinate singularity at $(r = 2M)$ can be eliminated by choosing a suitable coordinate system. In Schwarzschild spacetime, $r = 2M$ represents the event horizon, a spherical surface that distinct two regions of spacetime: BH interior and exterior. The event horizon is a null hypersurface, and the region within it is inappropriate to an outside observer. Eq. (1.11) and further analysis indicate that the escape velocity at this surface is equal to the speed of light.

The Schwarzschild metric is only valid in the gravitational source spacetime where $r > rs = 2M$. Previously regarded to be a non-physical solution, Schwarzschild BH is now recognized as a reality [1, 2]. The Schwarzschild solution is the static solution for EFEs because its components are independent of time coordinates and the metric remains constant when t changes from positive to negative $(t \to -t)$. In 1923, G. D. Birkho demonstrated that the Schwarzschild solution is the only vacuum solution for EFEs that explains a spherically symmetric body's gravitational field [21]. This argument is known as Birkho's theorem.

1.2.3 Reissner-Nordström Black Hole

The Reissner-Nordström black hole (RNBH) metric is a nonrotating, spherically symmetric static black hole solution to the Einstein-Maxwell equations. It defines the spacetime geometry of charged, nonrotating, spherical symmetric masses. The line element of the RNBH (in natural units) for a gravitational mass M with an electric charge Q in spherical coordinates is [1, 2].

$$ds^2 = -\left(1 - \frac{2M}{r} - \frac{Q^2}{r^2}\right) dt^2 + \left(1 - \frac{2M}{r} - \frac{Q^2}{r^2}\right)^{-1} dr^2 + r^2 d\theta^2 + r^2 \sin^2\theta d\phi^2. \quad (1.14)$$

The electromagnetic four-potential, which determines the electromagnetic field at every point in space, can be expressed as

$$A^\mu = \left(\frac{Q}{r}, 0, 0, 0\right). \quad (1.15)$$

The RNBH has two horizons $(r\pm)$ called outer and inner horizons, which are located in spacetime where $g_{rr} = 0$. Therefore, the RNBH horizons are situated at

$$r_\pm = M \pm \sqrt{M^2 - Q^2}, \quad (1.16)$$

where $M \leq Q$. In $M = Q$, the line elements represent the extremal BH with a single horizon. Furthermore, if $Q > M$, the line element Eq. (1.14) denotes an NS. The line element Eq. (1.14) has an essential singularity at $r = 0$, although the metric is not well-defined.

The BH $r\pm$ has coordinate singularities at its horizons. For zero charge $(Q = 0)$, the RNBH line element and other physical quantities are reduced to the Schwarzschild BH.

1.2.4 Kerr Black Hole

Roy Kerr developed the vacuum solution for EFEs in 1963, which explains spacetime outside of the spinning gravitational body. The Kerr BH is an axisymmetric, stationary solution. The Kerr solution, which describes spacetime outside a rotating object, is defined by two parameters: the angular momentum J and the mass M. The line element of the Kerr BH can be represented as [1, 2].

$$ds^2 = -\left(1-\frac{2Mr}{\rho}\right)dt^2 - \frac{4Mar\sin^2\theta}{\rho}d\phi dt + \frac{\rho}{\Delta}dr^2 + \rho d\theta^2 + \left(r^2+a^2+\frac{2Mra^2\sin^2\theta}{\rho}\right)\sin^2\theta d\phi^2, \tag{1.17}$$

where

$$\Delta = r^2 - 2Mr + a^2, \tag{1.18}$$

$$\rho = r^2 + a^2\cos^2\theta, \tag{1.19}$$

$$a = \frac{J}{M}. \tag{1.20}$$

The Kerr BH has two horizons, interior horizon r_- and exterior horizon r_+. These horizons are placed where $g_{rr} \equiv \Delta = 0$, resulting in

$$r_\pm = M \pm \sqrt{M^2 - a^2}, \tag{1.21}$$

with $M \geq a$. If $M = a$, the two horizons $r\pm$ of the Kerr BH merge, resulting in an extremal BH. If $a > M$, there is no BH, and the line element Eq. (1.17) denotes an NS. The Kerr BH has an essential singularity at $\rho = 0$, which is attainable for $\theta = \pi/2$ and $r = 0$. This represents the ring singularity in the equatorial plane. Unlike the Schwarzschild and RNBHs, the Kerr BH line element is not invariant under $t \to -t$ translation, making it non-static. Furthermore, due to the BH rotation, the Kerr BH spacetime is axisymmetric rather than spherically symmetric. The rotation of the BH causes frame-dragging effects, which will be examined further in the discussion.

1.2.5 Kerr-Newman Black Hole

In 1965, Ezra T. Newman proposed the Kerr-Newman black hole (KNBH) solution, which describes the geometry of spacetime outside a rotating charged object. The KNBH is characterized by three parameters: the object's charge (Q), mass (M), and angular momentum (J). The KNBH's line element is [1, 2].

$$ds^2 = -\frac{\Delta}{\rho}[dt - a\sin^2\theta d\phi]^2 + \frac{\rho}{\Delta}dr^2 + \rho d\theta^2 + \frac{\sin^2\theta}{\rho}[(r^2+a^2)d\phi - adt]^2, \tag{1.22}$$

where

$$\Delta = r^2 - 2Mr + Q^2 + a^2 \;\; and \;\; \rho = r^2 + a^2\cos^2\theta. \tag{1.23}$$

The electromagnetic field in spacetime is defined as the four-potential $one - form/covector^2$.

$$A_\mu dx^\mu = -\frac{Qr}{\rho}(dt - a\sin^2\theta d\phi), \tag{1.24}$$

The BH has two horizons that are genuine solutions to the problem.

$$r^2 - 2Mr + Q^2 + a^2 = 0, \tag{1.25}$$

and are given by

$$r_\pm = M \pm \sqrt{M^2 - Q^2 - a^2} \;\; with \;\; a^2 + Q^2 \leq M^2, \tag{1.26}$$

By definition, one form maps vectors to real values.

If $M^2 < a^2 + Q^2$, $r\pm$ is not real, and the line element Eq. (1.22) denotes an NS. The KNBH features an important ring singularity at $\rho = 0$, where $\theta = \pi/2$.When the charge Q is zero, the line element and other quantities are reduced to the Kerr BH. However, for zero rotation, the line element of the RNBH can be successfully obtained.

1.2.6 Event Horizon

According to physics, a body's mass and separation from its center of gravity define its escape velocity at a given location. A spacetime boundary known as an event horizon occurs when the escape velocity is greater than or equal to the speed of light. As light enters the event horizon, it cannot exit the BH. Communication between observers inside and beyond the event horizon is impossible, which prevents information from being shared.

1.2.7 Light Ring

A photon sphere appears at a point on a BHs event horizon where the force of gravity is so great that photons eliminated from the hole bend around it and return to their original location, giving the appearance of a boomerang.

$$r = \frac{3GM}{c^2} = \frac{3r_s}{2}. \tag{1.27}$$

1.2.8 Topological Number of Static Spheres

To determine W, the behaviour of vector ϕ at the boundary between the $r-\theta$ plane is examined. A straightforward computation shows that the path of ϕ is upward at $\theta = \phi$ and 0. When $r = r_h$, $f(r_h) = 0$, and $f(r > r_h) > 0$ are close to the horizon, ϕ is positive, indicating that ϕ is moving rightward in the plane, independent of ϕ^θ values. For an asymptotically flat black hole with huge r, $f(r)$ can easily approach zero. This suggests that ϕ is also moving to the right. The whole parameter space boundary is represented by the closed rectangular loop. The vector's direction is indicated by the black arrows. Along the boundary, the direction of the vector changes. A complete loop is not formed when the loop is turned counterclockwise. As a result, obtaining the entire topological number is simple.

$$W = 0 = \Sigma\omega_i. \tag{1.28}$$

Static spheres are always found in pairs for asymptotically flat, static, and spherically symmetric BHs. Radially stable and unstable static spheres have winding numbers of $w = 1$ and -1, respectively, and if one of them is radially stable, the other must be unstable. This conclusion varies for naked singularities. The winding number of the ith zero point of ϕ is represented by ω_i.

1.2.9 The Number of Static Sphere

The number of static spheres refers to the count of distinct regions around a black hole where objects can maintain a stationary position relative to the black hole rotation. These regions can vary in stability with some being stable and others unstable. Determining the number of static spheres for a black hole provides universal information about its structure, independent of specific space details [22].

1.2.10 Lagrangian Method for Geodesics

The geodesics in Euclidean space are straight lines with two comparable defining qualities, the tangent vector, which always points in the same direction along the line, represents the shortest path between two points. Geodesics can be defined in larger manifolds by generalizing either characteristic. In a pseudo-Riemannian manifold, both non-null and null geodesics can be defined by the fixed direction of their tangent vectors, while only non-null geodesics can be defined by the extremal length. Therefore, the evidence is not valid for null geodesics. Unfortunately, a variational approach can provide equations for affinely parameterized systems geodesics, which is still valid for null geodesics. A system is described by a set of generalized parameters x^a in classical mechanics, which are factors of time t. These coordinates define a space related to certain line elements.

$$ds^2 = g_{ab}dx^a dx^b. \tag{1.29}$$

In classical mechanics, this is known as the system's configuration space. The system's Lagrangian can be calculated by combining energies due to motion i.e. kinetic energy and due to position that is potential energies.

$$L = T - V = \frac{1}{2} g_{ab}\dot{x}^a \dot{x}^b - V(x), \tag{1.30}$$

here $\dot{x} \equiv dx^a/dt$.

$$S = \int_{t_i}^{t_f} L dt. \tag{1.31}$$

The Euler-Lagrange equations determine the equations of motion for a stationary system with little changes in the functions $x^a(t)$.

$$\frac{d}{dt}\left(\frac{\partial L}{\partial \dot{x}^a}\right) - \frac{\partial L}{\partial x^a} = 0. \tag{1.32}$$

The complete form of the equations of motion may appear less familiar.

$$\ddot{x}^a + \Gamma^a_{bc}\dot{x}^b \dot{x}^c = -g^{ab}\partial_b V. \tag{1.33}$$

These are the formulas for a geodesic that is affinely parameterized and has a force term on its right side. The metric associations of the space of configuration are represented in this case by the Γ^a_{bc}. According to Lagrange's equations, free particles in the configuration space travel along geodesics in the absence of forces. The 'Lagrangian' in a pseudo-Riemannian manifold may be studied to derive the mathematical equations for an affinely parameterized geodesic.

$$L = g_{ab}\dot{x}^a\dot{x}^b. \tag{1.34}$$

The results of putting this Lagrangian into the Euler-Lagrange equations are $\dot{x}^a = \frac{dx^a}{du}$, removing the unnecessary factor $\frac{1}{2}$.

$$\frac{d}{du}\left(\frac{\partial L}{\partial \dot{x}^a}\right) - \frac{\partial L}{\partial x^a} = 0. \tag{1.35}$$

yields, as needed.

$$\ddot{x^a} + \Gamma^a_{bc}\dot{x}^b\dot{x^c} = 0. \tag{1.36}$$

This calculation applies to null and non-null geodesics, as it does not require $\dot{s} \neq 0$. Euler-Lagrange equations can generate geodesic equations and their connection coefficients can be extracted from the latter. Consider using the first integral to solve the geodesic Eqs. (1.33). Null geodesics have a simple first integral.

$$g_{ab}\dot{x}^a\dot{x}^b = 0. \tag{1.37}$$

However, for non-null geodesics, if we choose the parameter $u = s$, then

$$\mid g_{ab}\dot{x}^a\dot{x}^b = 1 \mid . \tag{1.38}$$

These findings can be instrumental in solving the geodesic equations. Establishing the equivalence between the geodesic and Euler-Lagrange equations reveals a crucial insight: According to Eq. (1.29), if the metric g_{ab} does not depend on a particular coordinate x^d, then suggests that

$$\frac{\partial L}{\partial \dot{x}^d} = g_{db}\dot{x}^b = constant. \tag{1.39}$$

Using the equation $\dot{x}^b = t^b$, where t is the geodesics tangent vector, we may conclude that

$$t^d = constant. \tag{1.40}$$

During an affinely parameterized geodesic, the d^{th} covariant component t^d of the tangent vector remains constant if the metric parameters g_{ab} are independent on the coordinate x^d. This concept comes up again and again while studying particle motion in the context of GR.

CHAPTER 2

LITERATURE REVIEW

Newtonian gravitational theory, effectively explains the gravitational forces between bodies and how objects move around or toward these bodies. Newton's laws successfully provide the equation of trajectories of slowly moving bodies in the weak gravitation field. The relationship between gravity and objects trajectories in his gravitation theory. However, it does not explain the relationship between the velocities of objects moving at speeds comparable to the speed of light because, in his gravitational theory, he considers time as a universal quantity [23]. Einstein explained that time is not a universal quantity as in the Newtonian theory of gravity. In 1905, Einstein presented the theory of SR and addressed the concept of time dilation and length contraction and how high velocities can affect time and space [5]. Furthermore, Newtonian mechanics failed to accurately describe the orbit of Mercury around the Sun and the bending of light by gravity. Einstein's theory of GR resolved these issues presented in 1915 [1]. This theory relates the spacetime curvature to the distribution of mass and energy, including planets and stars, among other objects through a system of coupled differential equations known as EFEs [5]. These equations explain how mass and energy cause spacetime to bend, which in turn influences the motion of objects within this curved spacetime [24, 25]. This bending of spacetime is what we experience as gravity. If the mass-energy distribution is known, the EFEs provide information about the spacetime curvature and trajectories of other bodies in spacetime. This theory also helps in understanding gravity on a cosmic scale [25]. They have been essential in predicting and explaining phenomena such as BHs, GWs, and the expansion of the universe. A BH is an astronomical object with such strong gravity that its escape velocity exceeds the speed of light [5, 25]. Because light cannot escape its gravitational pull, BHs cannot be observed directly, which is why they were originally referred to as "dark stars" and later named "black holes" [25]. The concept of a BH was first proposed by John Michell in 1783 and independently by Marquis de Laplace in 1796 [7, 8]. Later, this idea was largely overlooked until Einstein presented his theory of general relativity because before Einstein it was not clear how light could be influenced by a gravitational field. Einstein provided a framework which explained that light can be influenced by a gravitational field as it always follows straightest a possible path in spacetime which can be curved due to the presence of gravitational objects. The first solution of EFEs presented by Karl Schwarzschild in 1916, also predicted the mysterious object "Black Hole".

Astronomically, A black hole forms when a massive star collapses under its gravity at the end of its life cycle [26]. Recent advancements in astronomical measurements and observational data strongly support the presence of supermassive BHs at the centres of these galaxies [18, 27]. Recently, astronomers captured the first image of a supermassive BH at the centre of our galaxy, the Milky Way [18, 27, 28]. This achievement, made possible by an international team of researchers known as the Event Horizon Telescope (EHT) collaboration, utilized a global network of radio telescopes [27, 28]. These findings provide compelling evidence for the existence of BHs at the centres of most galaxies. Therefore, studying the physics of black holes is important because they are important for understanding the structure of galaxies and the universe as a whole.

To study the motion of stars around compact objects like BHs, we have required the understanding of circular orbits around these objects [18, 29]. So, for that purpose, the timelike circular orbits (a path that is moving forward in time without escaping) around these objects and their stability analysis is a subject of interest [11]. The circular geodesics in a rotating charged the BH in the presence of PFDM has been studied in Ref. [30]. In the rotating BH spacetime, two kinds of circular orbits can be studied: the timelike and null orbits. For a timelike orbit, both charged and neutral particles are considered and the effective potentials are in further detail. The results show how the particle's energy E, angular momentum L, and effective potential V_{eff} are affected by the BHs charge Q, spin a, and PFDM parameter α. Furthermore, the Penrose process is examined to comprehend how negatively charged particles in the ergosphere could induce an energy gain for external particles. Recently, timeline circular orbits and their stability analysis have been done using topological classes [31, 32, 33]. The topological classes depend on the energy of the object to perform the stability analysis of the timelike circular orbit [34]. The circular orbits, if they exist always appear in pairs with constant angular momentum if they exist. Also like cyclical cycles, both unstable and stable times have positive or negative winding numbers [35]. Static spheres around black holes are regions where objects can remain still relative to BH rotation. They can be stable or unstable and their number provides universal information about BH structures [35].

Topology helps us to understand LRs that revolve around BHs. By calculating the topological charge it was observed that LRs can be well-defined [29, 36] and are related to the decay time of BHs and the formation of black shadows. The EHT collaboration [11, 37] and the Virgo collaboration [36] have just released fresh observations, which can be understood by topology approaches. The light ring is located at the vector's zero point, according to Gunha Berti's 2017 discovery of a unique vector that takes zero geodesics into account. Therefore, the winding numbers of zero points provide us with some relevant topological results in vector space. Using topological methods, we find that in a fixed space solid and an axially symmetrically balanced the topological value of the LRs, and the ultracompact object will be zero. All LRs are missing. This means that if LRs are present, they should appear in small pairs. Furthermore, if one LR is stable, it follows that the other must be unstable [38, 39]. The study was expanded later by adding the BH backgrounds [29]. For any rotating experience, the belief state is, that a desk-bound, asymptotically, axisymmetric, flat 4-dimensional spacetime of a BH has at least one universal LR off the horizon. Other associated problems which include angular movement stability have been discussed in references [31, 34]. At a positive cost of the dilatonic parameter, a topological segment transition was observed for the DM spacetime and the Schwarzschild DM BH [40]. We can combine this with the topological current map theory of Duan's [40] and extend the analysis of BHs to the non-rotating condition [35]. The topological charge was studied in the sense of inner structure, the phenomenon of bifurcation. Previous studies on the Dyonic black hole solution [33] have shown that many photon circles exist. The PSs, which are LRs' equivalents in spacetime with spherical symmetry. This presents an opportunity to test the nontrivial topological argument. It is our observation that the topological charge, independent of the other parameters, is always -1. Accordingly, regular PSs are always greater than unusual PSs. The topological charge remains unaffected by the spin of the black hole. The research led us to create an approach to topological BH thermodynamics [41].

CHAPTER 3

TOPOLOGY OF TIMELIKE CIRCULAR AROUND ROTATING BLACK HOLE

This chapter is devoted to studying the topology of a timelike equatorial circular orbit around a rotating black hole, as described in the Ref. [11]. For this study, a generic axisymmetric, stationary, asymptotically flat BH will be considered. A topological analysis of circular orbits in the spacetime will be conducted. Topology analysis (based on topological numbers) is a useful technique for analyzing the stability of circular orbits around black holes and compact objects. The topological analysis of LRs or null circular orbits (NCOs) has been extensively studied to investigate their properties [36, 29]. However, unlike the light ring, the circumference of the equatorial TCO depends on the angular momentum l and energy E of the test particles. It is shown that the energy and angular momentum of the test particles do not influence the asymptotic behaviour of the n-vector field at the zero points, which correspond to equatorial TCOs.

3.1 Circular Geodesics and Effective Potential

To investigate the topological analysis of LRs and TCOs consider the general stationary, axisymmetric, asymptotically flat BH spacetime. A 4-dimensional BH is called stationary if all the metric components $g_{\mu\nu}$ are independent of the t it is called axisymmetric if components are independent of ϕ coordinate. It is called asymptotically flat if the metric components $g_{\mu\nu} \to \pm 1$ whenever $r \to \infty$. Furthermore, the spacetime has a north-south pole symmetry. Due to this symmetry, the motion of a circular orbit can only occur within the equatorial plane. The generic metric with these conditions can be written as [11]

$$ds^2 = g_{tt}dt^2 + g_{rr}dr^2 + g_{\theta\theta}d\theta^2 + g_{\phi\phi}d\phi^2 + 2g_{t\phi}dtd\phi, \tag{3.1}$$

with the metric signature $(-,+,+,+)$. This metric can describe most of the known BHs. The BH horizon $r = r_h$ (where $(g_{rr})^{-1} = 0$) divides the whole region of spacetime into; the interior $0 \leq r < r_h$, and; the exterior $r_h < r < \infty$. Here assumed that g_{rr}, $g_{\theta\theta}$, and $g_{\phi\phi}$ are positive (> 0) with $\det(-g) > 0$ outside the horizon ($r_h < r < \infty$) and For simplicity, we denote:

$$B(r,\theta) \equiv g_{t\phi}^2 - g_{tt}g_{\phi\phi} > 0, \tag{3.2}$$

which is zero at the horizon that is, $B(r_h,\theta) = 0$. This notation helps in the coming discussion of particle motion.

The Hamiltonian approach will be used to study the topology of TCOs of a test particle around the generic black holes, which requires the Lagrangian of the test particle. The Lagrangian can describe the test particle's motion under metric Eq. (3.1) and is given as;

$$L = \frac{1}{2}g_{\mu\nu}\dot{x}^\mu\dot{x}^\nu = \frac{1}{2}\mu^2, \tag{3.3}$$

where the dot represents the derivative with respect to the affine parameter, while the spacelike, null, and timelike path are represented by $\mu^2 = -1$, 0, and 1, respectively. The conjugate momenta are computed as follows

$$\pi_\mu = \frac{\partial L}{\partial \dot{x}^\mu} = g_{\mu\nu}\dot{x}^\nu. \tag{3.4}$$

As a result, the Hamiltonian approach for the test particles is as follows

$$H = \pi_\mu \dot{x}^\mu - L. \tag{3.5}$$

Using the metric components Eq. (3.5), the Hamiltonian takes the following form

$$H = \frac{1}{2}\left(g_{tt}\dot{t}^2 + g_{rr}\dot{r}^2 + g_{\theta\theta}\dot{\theta}^2 + g_{\phi\phi}\dot{\phi}^2 + 2g_{t\phi}\dot{t}\dot{\phi}\right) = -\frac{1}{2}\mu^2. \tag{3.6}$$

or

$$g_{rr}\dot{r}^2 + g_{tt}\dot{t}^2 + g_{\theta\theta}\dot{\theta}^2 + g_{\phi\phi}\dot{\phi}^2 + 2g_{t\phi}\dot{t}\dot{\phi} + \mu^2 = 0. \tag{3.7}$$

The above equation can be considered as it has two terms that can be represented by the potential energy term V and kinetic energy term K as [42, 43].

$$K = g_{\theta\theta}\dot{\theta}^2 + g_{rr}\dot{r}^2, \tag{3.8}$$

$$V = g_{\phi\phi}\dot{\phi}^2 + 2g_{t\phi}\dot{t}\dot{\phi} + g_{tt}\dot{t}^2 + \mu^2. \tag{3.9}$$

As a result, the Eq. (3.7) becomes

$$V + K = 0. \tag{3.10}$$

It is important to note that, the kinetic energy is non-negative that is $K \geq 0$, and is zero only when $\dot{r} = \dot{\theta} = 0$ and in this case the particle's motion is defined the effective potential only. As the metric components $g_{\mu\nu}$ and hence the Lagrangian are independent of t and ϕ coordinates, therefore there exist two constant of motions; the energy E, and orbital angular momentum l of test particles along each geodesic. They can be defined in terms of the corresponding two Killing vectors, ψ^μ and ξ^μ, as follows

$$-E = g_{t\phi}\dot{\phi} + g_{tt}\dot{t} = g_{\mu\nu}u^\mu\xi^\nu, \tag{3.11}$$

$$l = g_{\phi\phi}\dot{\phi} + g_{t\phi}\dot{t} = g_{\mu\nu}u^\mu\psi^\nu, \tag{3.12}$$

Here u^μ indicates the geodesic tangent vectors define as $u^\mu = (\dot{t}, \dot{r}, \dot{\theta}, \dot{\phi})$. By solving these two given equations, one can be obtained

$$\dot{t} = \frac{1}{B}(g_{\phi\phi}E + g_{t\phi}l), \tag{3.13}$$

$$\dot{\phi} = -\frac{1}{B}(g_{t\phi}E + g_{tt}l). \tag{3.14}$$

Now eliminating $\dot{t}$ and $\dot{\phi}$ from an effective potential (3.9) takes the form,

$$V = g_{\phi\phi}\dot{\phi}^2 + 2g_{t\phi}\dot{t}\dot{\phi} + g_{tt}\dot{t}^2 + \mu^2. \tag{3.15}$$

or it can be written as

$$\begin{aligned} V = {} & g_{tt}\left[\frac{1}{B}(Eg_{\phi\phi} + lg_{t\phi})\right]^2 - 2g_{t\phi}\left[\frac{1}{B}\left(Eg_{\phi\phi} + lg_{t\phi}\right)\right]\left[\frac{1}{B}(Eg_{t\phi} + lg_{tt})\right] \\ & + g_{\phi\phi}\left[\frac{-1}{B}(Eg_{t\phi} + lg_{tt})\right]^2 + \mu^2, \end{aligned} \tag{3.16}$$

Taking B^2 common from Eq. (3.16)

$$V = \frac{1}{B^2}\left[E^2 g_{\phi\phi}(g_{\phi\phi}g_{tt} - g_{t\phi}^2) + 2Elg_{t\phi}(-g_{t\phi}^2 + g_{\phi\phi}g_{tt}) + l^2 g_{tt}(-g_{t\phi}^2 + g_{\phi\phi}g_{tt})\right] + \mu^2. \tag{3.17}$$

or

$$V = -\frac{1}{B}\left(E^2 g_{\phi\phi} + 2El g_{t\phi} + l^2 g_{tt}\right) + \mu^2. \tag{3.18}$$

This precisely reduces the potential of the photon for $\mu^2 = 0$. The effective potential can also be expressed as;

$$V = -\frac{l^2 g_{\phi\phi}}{B}\left(\frac{E^2}{l^2} + \frac{2E g_{t\phi}}{l g_{\phi\phi}} + \frac{g_{tt}}{g_{\phi\phi}}\right) + \mu^2, \tag{3.19}$$

or

$$V = \frac{-l g_{\phi\phi}}{B}\left(\frac{E}{l} - H_+\right)\left(\frac{E}{l} - H_-\right) + \mu^2, \tag{3.20}$$

where $H_\pm$ is just affected by the BH metric and stated by

$$H_\pm = \frac{-g_{t\phi} \pm \sqrt{B}}{g_{\phi\phi}}. \tag{3.21}$$

3.2 Topology of Light Rings

In this section, the topology of the light rings around the rotating BH will be discussed. For that purpose, we define effective potential Eq. (3.20) for photon and set $\mu^2 = 0$. In this case, the potential and its derivative vanish everywhere, that is, $V = \partial_r V = 0$, therefore, we can write

$$\left(\frac{E}{l} - H_+\right)\left(\frac{E}{l} - H_-\right) = 0, \tag{3.22}$$

which gives

$$H_\pm = \frac{E}{l}. \tag{3.23}$$

These results are consistent for LRs [42, 43]. The angular momentum's l and energy E of a photon are constant. Thus, we can express it as follows

$$\frac{\partial H_\pm}{\partial r} = 0. \tag{3.24}$$

The Eq. (3.24) must be solved to get the radius r_{LR} of the LR (sometimes called as photon sphere) for a stationary spherical BH. It can be seen that [see Eq. (3.21)], r_{LR} is independent of photon characteristics and it is related to the structure of the BH only, just like the black hole's horizon. Thus, the energy angular momentum ratio for photons orbiting along the LR is given by

$$\frac{E}{l} = H_{\pm}(r_{LR}). \tag{3.25}$$

Now, to discuss the topology of the LR, the n vector field is defined as [29].

$$v = \left(\frac{\partial_r H_{\pm}}{\sqrt{g_{rr}}}, \frac{\partial_\theta H_{\pm}}{\sqrt{g_{\theta\theta}}} \right). \tag{3.26}$$

This can be determined by computing the winding number of n vector field. The universal properties of a light ring in a BHs surroundings can be determined by analyzing the asymptotic behaviour of n vector field at the boundary, considering all regions (r, θ). The main advantage of this approach is that $H_{\pm}$ remains unaffected by the photon's energy or angular momentum. However, for TCOs, the situation becomes more complicated due to the existence of μ^2 the additional term in Eq. (3.20). Consequently, the next section will provide a detailed analysis of this scenario.

3.2.1 Timelike Circular Orbits

A TCO is a stable path taken by a massive object around a massive body that allows the object to experience proper time while maintaining a constant distance from the center mass. To discuss the topology of TCOs, It can be re-express as the effective potential Eq. (3.18) in the following way

$$V = -\frac{g_{\phi\phi}}{B} \left(E^2 + \frac{2El g_{t\phi}}{g_{\phi\phi}} + \frac{l^2 g_{tt} + B\mu^2}{g_{\phi\phi}} \right), \tag{3.27}$$

which can also be expressed as

$$V = -\frac{g_{\phi\phi}}{B}(E - e_1)(E - e_2), \tag{3.28}$$

where e_1 and e_2 are define as

$$e_{1,2} = \frac{-l g_{t\phi} \pm \sqrt{B}\sqrt{l^2 + \mu^2 g_{\phi\phi}}}{g_{\phi\phi}} \tag{3.29}$$

This results shows that TCOs with $V = 0$ determine the test particle's energy as

$$E = e_{1,2}. \tag{3.30}$$

For BH $g_{\phi\phi} > 0$ and $B \equiv g_{t\phi}^2 - g_{tt}g_{\phi\phi} > 0$, can be easily proved that

$$e_2 < \frac{g_{t\phi}}{g_{\phi\phi}}(|l| - l). \tag{3.31}$$

For $e_2 < 0$ is easily obtained for $l \geq 0$ and $0 > -2lg_{t\phi}/g_{\phi\phi} > e_2$ for $l < 0$ because of negative $g_{t\phi}$. As a result, the value of e_2 is negative for each value of l, so we ignore this case and only consider the case of e_1. Now in this case, the conditions we are $V = \partial_r V = 0$ which determine the conditions for TCO as follows

$$E = e_1, \tag{3.32}$$

$$\partial_r e_1 = 0. \tag{3.33}$$

As compared to the LR, $\partial_r e_1$, in this case, depends on both energy E and the test particle's angular momentum l, suggesting that the topology for the TCO cannot be constructed as for the photon light ring. However, similar to that of a photon light ring solving Eq. (3.32), we can determine the radius of the TCO if the angular momentum l is known. The angular momentum l does not influence the existence of a solution to the equation. After calculating the TCO's radius and putting it into Eq. (3.32), the test particle's energy can be determined. Here angular momentum values that maintain the asymptotic behaviour of $\partial_r e_1$ at the boundary of the (r, θ) plane for the global topology. To deal with this, the vector field $\phi = (\phi^\theta, \phi^r)$, similar to the vector used for photons as in Ref. [29] can be defined as +

$$\phi^\theta = \frac{\partial_\theta e_1}{\sqrt{g_{\theta\theta}}}, \quad \phi^r = \frac{\partial_r e_1}{\sqrt{g_{rr}}}. \tag{3.34}$$

Here the upper indexes are used to be consistent with the notations of [44]. It is clear that the expected value is $\theta = \pi/2$, with the TCO represented by $\phi = 0$. The analysis of the asymptotic behaviour of ϕ in the (r, θ) plane boundary illustrates the importance of the topological construction for the TCO.

The terms $g_{tt}^0, g_{\rho\rho}^0$, and b_0 are constant, and n is a natural number. One must have $n \geq 2$ given C^2 smooth and symmetry at the axis [45]. Using these into Eq. (3.29), yield the result

$$e_1 \sim \frac{\sqrt{-g_{tt}^0 l^2 \rho^2 + \sqrt{-g_{tt}^0}\mu^2 \rho^3}}{\rho^2}. \tag{3.35}$$

At dominant order in ρ, we have $g_{\theta\theta} d\theta^2 \sim g_{\rho\rho} d\rho^2$.

$$\phi^\theta \sim -sign\left(\frac{d\rho}{d\theta}\right) \frac{|l|\sqrt{-g_{tt}^o}}{\rho^2} \sim sign\left(\frac{d\rho}{d\theta}\right) \partial_\rho e_1, \tag{3.36}$$

$$\phi^{\theta} \sim -sign\left(\frac{d\rho}{d\theta}\right)\frac{(-g^{o}_{tt})^{\frac{1}{4}}\mu^{2}}{2\rho^{\frac{3}{2}}} \sim sign\left(\frac{d\rho}{d\theta}\right)\partial_{\rho}e_{1}, \tag{3.37}$$

representing the non-vanishing and vanishing angular momentum l cases respectively. As a result, ϕ^{θ} diverges when $\rho \to 0$, and its behaviour at small ρ does not depend on the angular momentum. When this is paired with $\rho^{-1} \sim \phi^{r}$, we obtain $\phi^{r} < \phi^{\theta}$. This suggests the line vector moves vertically between $\theta = 0, \pi$. Additionally, it is noted that the vector points outward at $\theta = 0$ and π, with $\frac{d\rho}{d\theta}$ being positive as $\theta \to 0$ and negative as $\theta \to \pi$. (ii) Horizon limit: The objective is to analyze the behaviour of the vector ϕ as r approaches r_h. According to Ref. [29], a local radial point x exists near the BH horizon, where $x = 0$ and $g_{xx} = 1$. The function can be analyzed in closeness to the horizon.

$$g_{\phi\phi} \backsimeq g^{H}\phi\phi + \mathscr{O}(x^{2}) \quad \omega \backsimeq \omega_{H} + O(x^{2}), \tag{3.38}$$

$$B \backsimeq g^{H}_{\phi\phi}k^{2}x^{2}, \quad g_{t\phi} \backsimeq -\omega_{H}g^{H}_{\phi\phi}, \quad g_{tt} \backsimeq \omega^{2}_{H}g^{H}_{\phi\phi}, \tag{3.39}$$

If the black hole's surface gravity is represented by κ, and the parameter $\omega = -g_{t\phi}/g_{\phi\phi}$ expanding in the terms of x, $g^{H}_{\phi\phi}$ and ω_{H} provide the dominating contributions at leading order gives the result

$$\partial_{x}e_{1} \backsimeq \kappa\sqrt{\frac{l^{2}}{g^{H}_{\phi\phi} + \mu^{2}}} + \mathscr{O}(x). \tag{3.40}$$

By applying the relation $(1/\sqrt{g_{rr}})(\partial/\partial r)$=$(1/\sqrt{g_{xx}})(\partial/\partial_{x})$, one can obtain

$$\phi^{r} = \frac{\partial_{r}e_{1}}{\sqrt{g_{rr}}} \backsimeq \kappa\sqrt{\frac{l^{2}}{g^{H}_{\phi\phi}} + \mu^{2}}. \tag{3.41}$$

For a non-extremal BH with positive surface gravity $\kappa > 0$, ϕ^{r} is positive. The direction of vector field π near the horizon, its component π^{θ} in angular direction θ will required. However, regardless of whether ϕ^{θ} is positive or negative, the vector ϕ should be oriented to the right, possibly with a slight inclination.

(iii) Asymptotic limit: The vector's behaviour at infinity will now be examined. At long distances, spacetime typically becomes flat in standard spherical dimensions.

$$g_{t\phi} \backsimeq -\mathscr{O}\left(\frac{1}{r}\right), \quad g_{\phi\phi} \backsimeq r^{2}\sin^{2}\theta + \mathscr{O}(1), \tag{3.42}$$

$$g_{tt} \backsimeq -1 + \frac{2M}{r} + \mathscr{O}\left(\frac{1}{r^{2}}\right), \quad g_{rr} \backsimeq 1 + \frac{2M}{r} + \mathscr{O}\left(\frac{1}{r^{2}}\right). \tag{3.43}$$

In asymptotically flat spacetime, the parameter M is a positive quantity signifying the mass of the black hole. Therefore, we have

$$\phi^r \backsimeq \frac{M\sqrt{\mu^2}}{r^2} + \mathscr{O}\left(\frac{1}{r^3}\right), \tag{3.44}$$

which has a positive but small value at equatorial plane $\theta = \pi/2$. The exact value of ϕ^θ can therefore be ignored. The vector ϕ indicates the horizon limit, which points towards the right. Finally, our method demonstrates that the angular momentum l of the test particle does not influence the behaviour of the vector ϕ at the boundary of the (r,θ) plane. This implies that creating a topology for huge particle TCOs in such a situation might be possible.

3.3 Local and Global Typologies

This study explores the local and global topological properties of TCOs by analyzing the behaviour of ϕ as it approaches the boundary of the (r,ϕ) plane. Additionally, it analyzes the topological structures of the ISCO and MSCO.

3.3.1 Global Property

The zero points of the vector field ϕ correspond to the locations of TCOs is demonstrated. One can compute the topological number W using the method described in [44] which suggested that for TCOs, the topological number is defined as

$$W = \int_\Sigma j^o d^2x. \tag{3.45}$$

for the TCOs in a certain area Σ within the (r,θ) plane and j^o is the zeroth component of the topological current defined as:

$$j^\mu = \frac{1}{2}\varepsilon^{\mu\nu}\varepsilon_{ab}\frac{\partial n^a}{\partial x^n u}\frac{\partial n^b}{x^\rho}, \tag{3.46}$$

with $x^o = t$ being a time control parameter the unit vectors $n^a = (n^r, n^\phi) = (\phi^\theta/|\phi|, \phi^r/|\phi|)$ and x^μ are the spacetime coordinates. As expected, that parameter can be used to study the evolution of zero points. Furthermore, additional particle or BH properties may be used as

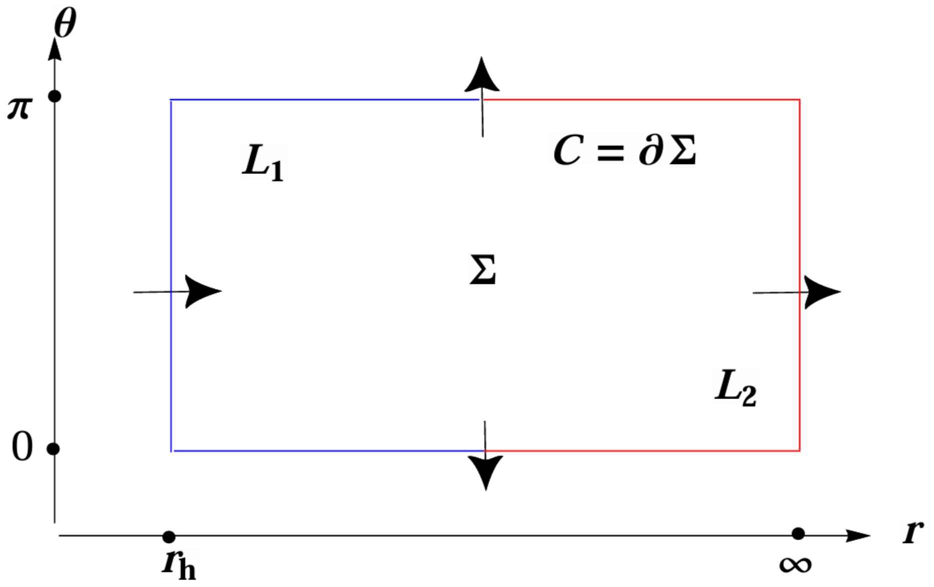

Figure 3.1: The parameter space Σ on the (r,θ) plane is enclosed by the contour $C = L_1 \cup L_2 = \partial\Sigma$, as depicted in Fig. 3.1. The right and left sections of the contour are represented by L_1 and L_2, highlighted in red and blue, respectively. The black arrows denote the estimated values of the vector ϕ along the boundary.

control parameters. For a definition to be appropriate, zero points must not cross the (r,ϕ) plane's boundary while the control parameter is finite.

The angular momentum l of the particle is utilized as a control parameter in this analysis. A brief explanation regarding the selection of energy will also be provided. After performing some calculations, the result corresponds to the findings in [44].

$$W = \sum_{n=1}^{N} w_n. \tag{3.47}$$

In the Σ region, this denotes W is the total winding number across all zero points. As x^μ occurs clockwise around the closed curve $\partial\Sigma$, count the number of loops generated by the vector x in the vector field ϕ to find the topological charge of the Σ area.

$$W = \frac{1}{2\pi}\oint_C \epsilon_{ab} n^a dn^b = \frac{1}{2\pi}\oint_C d\Omega. \tag{3.48}$$

The symbol Ω represents a change in vector direction. The entire parameter space is bounded by the curve $C = \partial\Sigma$, which illustrates the global topological properties.This closed curve can be divided into two distinct segments, L_2 and L_1, resulting in $C = L_2 \cup L_1$. Fig. (3.1), the vector disregards all angles, pointing exterior at $\theta = 0$ and π, and to the right at $r = \infty$ and r_h. Easily obtained from the asymptotic behaviour of ϕ.

$$W = \frac{1}{2\pi}\int_{L_1} d\Omega + \frac{1}{2\pi}\int_{L_2} d\Omega, \tag{3.49}$$

$$= \frac{1}{2\pi}\times(-\pi) + \frac{1}{2\pi}\times(\pi) = 0. \tag{3.50}$$

This suggests that the TCO's total topological number is zero. The result is universal, unaffected by the BHs spin or the angular momentum of the massive test particle. This remarkable result indicates that, in 4-dimensional stationary, asymptotically flat black holes, axisymmetric, TCOs with a given angular momentum consistently appear in pairs. Unlike the LR, which possesses a topological number of -1, implying the presence of at least one LR. This characteristic is distinctly different. For TCOs, the overall topological number disappears at $\theta = 0$ and π, where the vector ϕ points outside. As shown in Fig. 3.7(a), even if the vector ϕ is directed inside at $\theta = 0$ and π, the topological number can still vanish despite the presence of North-South pole Z_2 symmetry. The topological number W remains 0 even after the vector ϕ changes direction. However, removing the Z_2 symmetry allows for a more thorough exploration of the complete topological number. We further demonstrate these two possible scenarios, when Z_2 symmetry is broken, as illustrated in Figs. 3.7(b). Remarkably, we still observe

$$W = 0. \tag{3.51}$$

In both scenarios where Z_2 symmetry is either present or absent, the result $W = 0$ consistently applies.

3.3.2 Stability and Local Property

As stated before, it is verified that the TCOs have a zero global topological number. They might disappear or show up in pairs. The TCOs are dependent on the characteristics of the BH as well as the test particle, compared to the light ring, which symbolizes the intrinsic structure of spacetime. At some levels of angular momentum and energy, the TCOs may occur, but not at others. The local topological charge and stability of the TCOs are the main topics of this subsection. Since the energy and angular momentum of each of the TCOs are interconnected, they must satisfy the requirements stated in Eqs. (3.32) and (3.33) at any given radius r_t. From Eq. (3.33), the angular momentum can be solved as [46].

$$l_{\pm} = \frac{g_{t\phi}+g_{\phi\phi}\Omega_{\pm}}{\sqrt{\beta_{\pm}}}|_{r_t}, \tag{3.52}$$

where

$$\Omega_{\pm} = \frac{-\acute{g}_{t\phi} \pm \sqrt{C}}{\acute{g}_{\phi\phi}}, \tag{3.53}$$

$$\beta_{\pm} = -g_{\phi\phi}\Omega_{\pm}^{2} - 2g_{t\phi}\Omega_{\pm} - g_{tt}, \tag{3.54}$$

$$C = (\acute{g}_{t\phi})^{2} - \acute{g}_{tt}\acute{g}_{\phi\phi}. \tag{3.55}$$

The prime represents the derivative of the radial coordinates. The energy can be obtained by substituting the angular momentum l into equation (3.32).

$$E_{\pm} = -\frac{g_{tt} + g_{t\phi}\Omega_{\pm}}{\sqrt{\beta_{\pm}}}|_{r_t}. \tag{3.56}$$

Using Eq. (3.28), we've

$$\frac{\partial^2 V}{\partial r^2} = \frac{(e_1 - e_2)g_{\phi\phi}\sqrt{g_{rr}}}{B}\frac{\partial \phi^r}{\partial r}, \tag{3.57}$$

$$E = e_1. \tag{3.58}$$

Using Eq. (3.28), we obtain the results for the TCOs. The coefficient of variation is positive if $e_2 < 0$. That makes it simple to know.

$$\frac{\partial^2 V}{\partial r^2}|_{r_t} > 0(<0) \Rightarrow \frac{\partial \phi^r}{\partial r} > 0(<0)|_{r_t}. \tag{3.59}$$

Fig. 3.3 illustrates the direction of the vector ϕ along the contours, indicating two zero points at r_2 and r_1. The values of $\partial^2 V/\partial^2 r^2$ indicate stability, with positive values corresponding to stable TCOs and negative values to unstable TCOs. To assess the radial stability of the timelike circular orbits for ϕ_r, By using this Eq. (3.59). Assuming $r_1 < r_2$, Fig. 3.3 shows two TCOs at r_1 and r_2. We can determine ϕ_r by observing its asymptotic behaviour at the infinity and horizon. The values of ϕ_r are negative (r_1, r_2) and positive $(r_h, r_1) \cup (r_2, +\infty)$. the $\partial \phi^r/\partial r$ is positive near $r = r_2$ and negative near $r = r_1$. It shows that for r_1, the TCO is unstable, and it is stable at r_2. We want to take a brief look at local stability concerning the angle. Only equatorial the TCO with $\theta = \pi/2$ are examined. As Section 3.1 shows, the vector's central limit at $\theta = 0$, and π is not impacted by the presence of l. Furthermore, we found that TCOs had the same vertical stability as LRs Refs. [29, 31] demonstrate that TCOs are vertically stable. After assessing TCO stability, we need to analyze the winding numbers of the two TCOs. Examine the component ϕ^r of the vector ϕ, also referred to as n^r. The sign of the unit vector n changes at r_2 and r_1 as shown in Fig. 3.3. The vector's direction is also indicated. The winding numbers of 1 and -1 are determined by the change in vector direction at the zero points r_2 and r_1, respectively. Hence, stable TCOs are associated with positive winding numbers, whereas unstable TCOs have negative winding numbers. However, the overall winding number cancels out to zero.

3.3.3 Bifurcation Point and MSCO

The stable or unstable TCO is indicated by positive or negative winding numbers, where $\partial^2 V/\partial r^2 > 0$ or < 0. There is another critical case between the two mentioned cases with $\partial^2 V/\partial r^2 = 0$, corresponding to the Kerr-like BH ISCO or MSCO. Distinctions between the MSCO and the ISCO for hairy BHs and ultracompact objects, respectively, are given in References [46, 47, 48]. By using a sequence of stable TCOs, the MSCO stands for the stable TCO with the shortest radius that may be extended to spatial infinity. In Eq (3.55), the ISCO, represented by $C = 0$, is a small-radius stable TCO. For Kerr BHs and Schwarzschild, the MSCO and ISCO are the same. However, boson stars, proca stars, rotating hairy black holes, or nothing from them. This follows the procedure described in Ref. [46] to prevent misunderstandings. Usually, the MSCO is described as

$$V = 0, \quad \frac{\partial^2 V}{\partial r^2} = 0 \quad \frac{\partial V}{\partial r} = 0. \tag{3.60}$$

The first criterion is satisfied by setting $E = e_1$, which depends on the angular momentum l and radius r_t of the TCOs. The second equation, when solved, provides the radius r_t. Consequently, we represent the result as $r = r_t(l)$. Since the radius of TCO orbits varies with l, angular momentum acts as a control parameter. The third criterion can be determined through a straightforward calculation, which involves finding when $\partial^2 V/\partial r^2 = 0$ or $\partial\phi/\partial r^2 = 0$. This results in:

$$\frac{dl}{dr_t} = 0. \tag{3.61}$$

The Duan's topological current theory addresses this point (l^*, r_t^*). The MSCO associated point (t) represents one type of bifurcation. In this region, the angular momentum can be extended.

$$l - l^* = \frac{1}{2}\frac{d^2 l}{dr_t^2} \quad (r_t - r*_t)^2 + \mathscr{O}(r_t - r*_t)^3. \tag{3.62}$$

Two branches solutions on the $r_t - l$ plane result from this equation. When $\frac{d^2l}{dr_t^2} > 0$. If $l > l^*$, the two branch solutions are present, otherwise they are not. The bifurcation point can be classified as either created or annihilated [49]. Let us focus on the MSCO's topological number. Take the BP_2 branch, depicted as the blue curve in Fig. (3.9), which demonstrates the presence of two TCOs at high angular momentum and the absence of the TCOs at low angular momentum. This suggests that the point BP_2 is produced. The TCOs with large radii are stable, while those with small radii are unstable for a fixed angular momentum, corresponding to positive and negative winding numbers $w = -1$ and $w = 1$, respectively. Consequently, the higher branch has a positive one, while the lower branch has a negative winding number. The branches, with both positive and negative slopes corresponding to $\partial^2 V/\partial r^2 > 0$ and < 0, are visible and have winding numbers $w = -1$ and 1, respectively. For large angular momentum l, the higher branch exhibits $\partial^2 V/\partial r^2 > 0$, while the lower branch shows $\partial^2 V/\partial r^2 < 0$. As the angular momentum drops, this behaviour occurs. But the pattern alters after BP_2 is reached. The two branches merged, leaving a single MSCO with $\frac{\partial^2 V}{\partial r^2} = 0$ leaves. The MSCO might be considered a degraded timelike circular orbit. The MSCO breaks into two TCOs with $w = 1$ and $w = -1$, respectively, for angular momentum that is somewhat more than BP_2. Under the assumption that $\frac{\partial^2 V}{\partial r^2} > 0$ and < 0, $w = +1$ and -1 correspond to this. $w = +1$ or -1 are not accepted by the MSCO for $\frac{\partial^2 V}{\partial r^2} = 0$. Consequently, $w = 0$ must exist in the MSCO. The result is identical to that of Ref [44]. The MSCO's topological charge disappears. This can be further verified by analyzing the change in vector direction around the closed loop, as illustrated in Figs. 4.4(a) and 4.4(c).

3.4 Timelike Circular Orbit and Topology in Kerr Black Hole

The topological structure for TCOs in a general BH environment in the previous section. Here, we utilize this framework to investigate the spacetime features of the Kerr BH [50]. This will help us to understand the particular characteristics of a specific example.

3.4.1 Effective Potential of a Kerr Black Hole

The line element of the Kerr BH spacetime is given as

$$ds^2 = -\frac{\Delta}{\rho^2}\left(dt - a\sin^2\theta d\phi\right)^2 + \frac{\rho^2}{\Delta}dr^2 + \rho^2 d\theta^2 + \frac{\sin^2\theta}{\rho^2}\left[adt - (r^2+a^2)d\phi\right]^2. \quad (3.63)$$

where

$$\rho^2 = r^2 + a^2\cos^2\theta, \quad (3.64)$$

$$\Delta = r^2 - 2Mr + a^2. \quad (3.65)$$

The BH horizons can be determined by solving the equation $\Delta = 0$.

$$r_\pm = M \pm \sqrt{M^2 - a^2}. \quad (3.66)$$

The parameters must satisfy $a \leq M$ for the BH. From Eq. (3.28), we can obtained $e_{1,2}$ for Kerr BH background as

$$e_{1,2} = \frac{2laMr \pm \csc\theta\rho\sqrt{\Delta\left(\sin^2\theta(r^2+a^2)^2 - \Delta a^2\sin^4 + l^2\rho^2\right)}}{(r^2+a^2)^2 - \Delta a^2\sin^2\theta}, \quad (3.67)$$

where $\mu^2 = 1$ has been chosen for simplicity. These results simplify to $\theta = \pi/2$ on the equatorial plane.

$$e_{1,2} = \frac{2laMr \pm r\sqrt{\Delta((r^2+a^2)^2 + r^2l^2 - \Delta a^2)}}{(r^2+a^2)^2 - \Delta a^2}. \quad (3.68)$$

It can be observed that the typical behaviour of the potential in Fig. 3.4-3.6 for a BH with $M = 1$ and $a = 0.98$. As shown in Fig. 3.4 (a), for fixed energy E and $l = -4.5$, there are two extremal positions. There is one point with $E = 0.9691$ and $E = 0.99776$. For any curve, there is exactly one point $V = \partial_r V = 0$. These represent the regions where the radial velocity of surrounding particles is zero, indicating two TCOs for $l = -4.5$. Similarly, Fig. 3.4(b) shows two extreme points for a lower energy value when the angular momentum is increased to $l = -4.2209$. As the energy increases, these two extremal points converge at the black dot for energy $E = 0.9620$, satisfying the condition $\partial_r V = 0$. As expected, the MSCO is shown by the black dot. It is significant that this MSCO precisely matches the ISCO for the Kerr BH is particularly remarkable. There will be no extreme point when the energy exceeds 0.9620. In Fig. 3.5, it illustrates the effective potentials for $l = -4$ and $l = 1.5$, respectively.

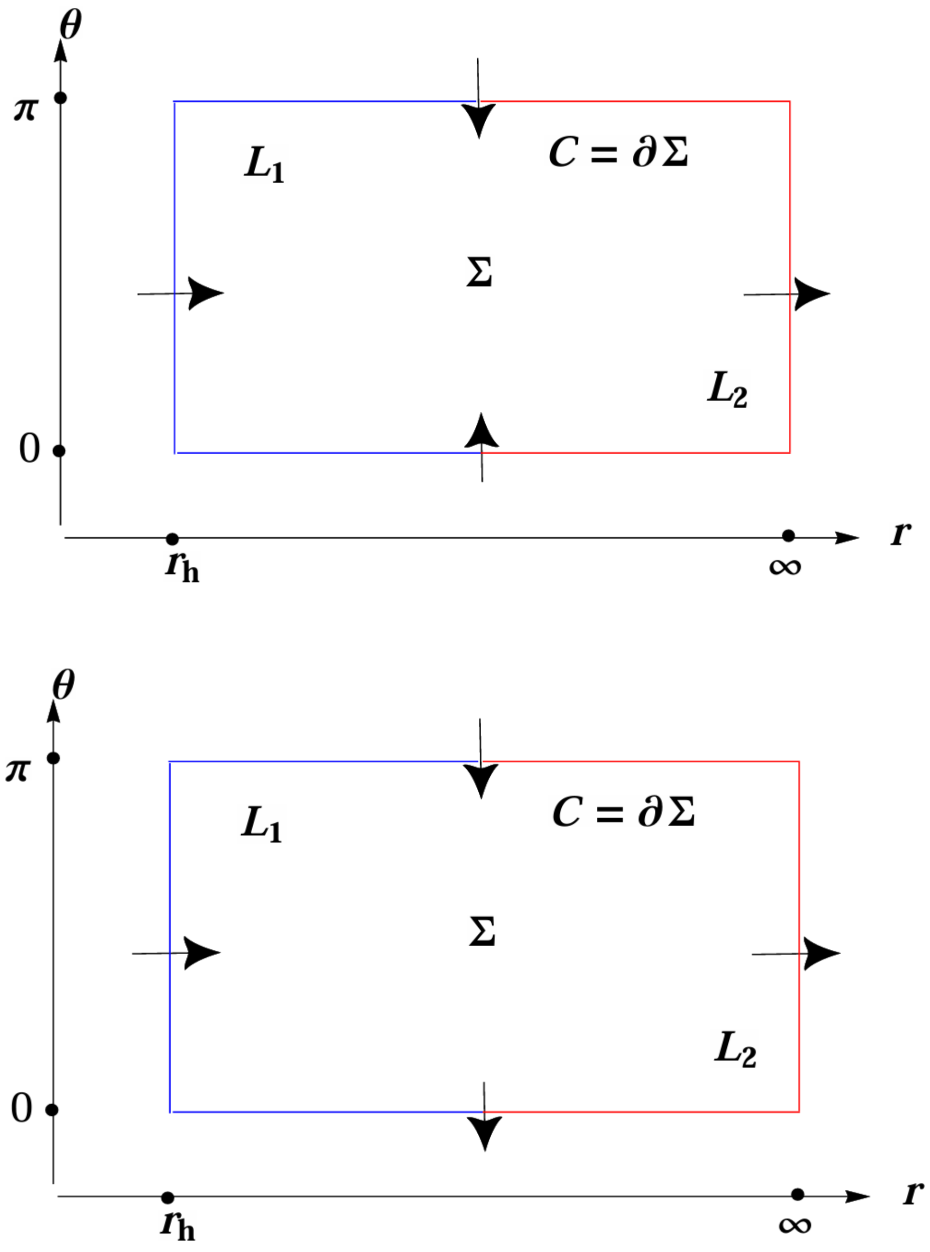

Figure 3.2: Changes in the direction of the vector ϕ at $\theta = 0$ and π.

The angular momenta display similar patterns, even though their signs are opposite. The absence of extremal points, regardless of energy changes, suggests that TCOs are not present in these cases. The effective potential is given in Fig. 3.5 for $l = 1.6827$. a similar pattern to that shown in Fig. 3.6 (a). The MSCO exists for particular values of E, l, and a.

Fig. 3.6 (a) shows two TCOs for $l = 1.7$, denoted by black dots. These display the standard behaviour associated with the effective potential. Consequently, by adjusting the angular momentum, we can observe either two TCOs, a single MSCO, or the absence of any TCOs.

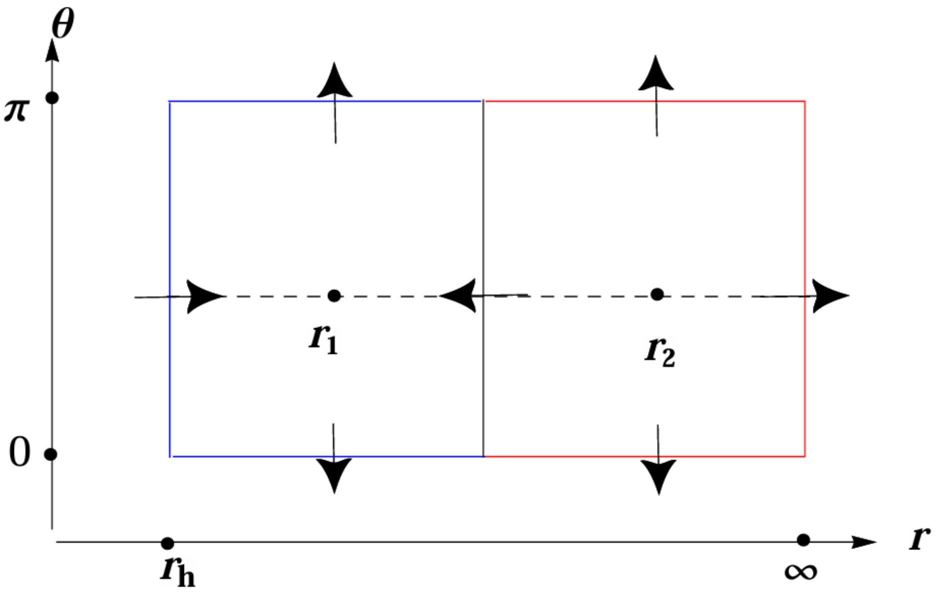

Figure 3.3: This shows how the vector π is represented along the contours that surround the two zero points at r_1 and r_2.

3.4.2 Asymptotic Behaviours and Vector

The vector's zero points match the above-depicted timelike circular orbits. The aim is to investigate whether the vector's asymptotic behaviour in the context of a Kerr BH is consistent with the general case described in Section II. The complex procedure will not be analyzed here, but it is possible to create the vector using Eq. (3.34). Upon approaching $\theta = 0$, the subsequent behaviour of the vector is

$$\phi^r = \frac{\partial_r e_1}{\sqrt{g_{rr}}}, \tag{3.69}$$

$$\phi^r(\theta \to 0) = \frac{(a^2(M+r) - l + (-3M+r)r^2)}{(r^2+a^2)^{\frac{5}{2}}}\theta^{-1} + \frac{2l\sqrt{\Delta}aM(-3r^2+a^2)}{(r^2+a^2)^{\frac{7}{2}}} + O(\theta), \tag{3.70}$$

$$\phi^\theta = \frac{\partial_\theta e_1}{\sqrt{g_{\theta\theta}}}, \tag{3.71}$$

$$\begin{aligned}\phi^\theta(\theta \to 0) = {} & \frac{-l\sqrt{\Delta}}{(r^2+a^2)^{\frac{3}{2}}}\theta^{-2} \\ & + \frac{\sqrt{\Delta}(3a^6 + (-2l^2+9r^2)a^4 + a^2r(9r^3 - l^2(r+12M)) + r^4(3r^2+l^2))}{6l(r^2+a^2)^{\frac{7}{2}}} + O(\theta),\end{aligned} \tag{3.72}$$

Moreover, nearly $\theta = \pi$, we've

$$\phi^r(\theta \to \pi) = \frac{l(a^2(r+M)+r^2(-3M+r))}{(a^2+r^2)^{\frac{5}{2}}}(\theta-\pi)^{-1} + \frac{2l\sqrt{\Delta}aM(3r^2+a^2)}{(r^2+a^2)^{\frac{7}{2}}} + O(\theta-\pi), \tag{3.73}$$

$$\begin{aligned}\phi^\theta(\theta \to \pi) = &-\frac{\sqrt{\Delta}(3a^6+a^4(9r^2-2l^2)+a^2r(9r^3-l^2(12M+r))+r^4(l^2+3r^2))}{6l(a^2+r^2)^{\frac{7}{2}}}\\ &+\frac{l\sqrt{\Delta}(\theta-\pi)^{-2}}{(a^2+r^2)^{\frac{3}{2}}}+O(\theta-\pi),\end{aligned} \tag{3.74}$$

$$\begin{aligned}\phi^\theta(\theta \to \pi) = &\frac{l\sqrt{\Delta}}{(r^2+a^2)^{\frac{3}{2}}}(\theta-\pi)^{-2}\\ &-\frac{\left[\sqrt{\Delta}(3a^6+(-2l^2+9r^2)a^4+ra^2(9r^3-l^2(r+12M))+r^4(3r^2+l^2))\right]}{6l(r^2+a^2)^{\frac{7}{2}}}+O(\theta-\pi).\end{aligned} \tag{3.75}$$

As a result, the vector's direction $arg\phi = arctan(\phi^\theta/\phi^r)$ when $\theta = \pi$ and $\theta = 0$ is

$$arg\phi(\theta \to 0) \sim arctan(-\theta^{-2}) \sim arctan\left(\frac{-l\sqrt{\Delta}}{(a^2+r^2)^{\frac{3}{2}}}\theta^{-2}\right) = \frac{-\pi}{2}, \tag{3.76}$$

$$arg\phi(\theta \to \pi) \sim arctan(\theta^{-2}) \sim arctan\left(\frac{l\sqrt{\Delta}}{(a^2+r^2)^{\frac{3}{2}}}\theta^{-2}\right) = \frac{\pi}{2}. \tag{3.77}$$

As a result, the vector's position is downward at $\theta = 0$ and upward at $\theta = \pi$. we can further extend the vector at large r on the equatorial plane, which gives

$$\phi^r(\theta = \frac{\pi}{2}, r \to \infty) = \frac{M}{r^2} - \frac{l^2}{r^3} + O\left(\frac{1}{r^4}\right). \tag{3.78}$$

The modest positive parameter $\in = r - r_h$ is denoted near the horizon. The vector is then expanded near the horizon to give us

$$\phi^r(\theta = \frac{\pi}{2}, \in \to 0) = \frac{\sqrt{(-a^2+M^2)(M^2+l^2)}(M-\sqrt{-a^2+M^2})}{4M^2a^2} + O(\in^{\frac{1}{2}}). \tag{3.79}$$

The positive nature of the zero-order is important. At both the horizon and large values of r, the vector points to the right, as $\phi^\theta(\theta = \pi/2) = 0$. For example, when a is zero, we find that

$$\phi^r(\theta = \frac{\pi}{2}, r \to r_+) = \frac{1}{4M}\sqrt{\frac{l^2}{4M^2}+1}. \tag{3.80}$$

The position of the unit vector n for $M = 1$, $l = 1.5$, and $a = 0.98$ is illustrated in Fig. 4.4 with $g^H_{\phi\phi} = 4M^2$ and $\kappa = 1/4M$, the Schwarzschild BH yields the exact result given in Eq. (3.41). The

Eq. (3.41) gives the specific result. In conclusion, the previously discussed general framework matches the asymptotic behaviour of the vector in the Kerr BH scenario. This indicates that the total number of timelike circular orbits in the Kerr BH background is necessarily 0.

Here, findings is briefly summarize, as the process is similar. The topological number W is zero for prograde and retrograde TCOs when $E \in (0,1)$. However, $W = -1$ arises for energies greater than one, specifically at $E = 1$. This change occurs because, as energy exceeds $E = 1$, the positions of vectors $\phi^r_{1,2}$ at a large distance r shift. For both directions of rotation, a topological phase transition occurs at $E = 1$. Particles with $E < 1$ have finite velocities and cannot reach infinity in an asymptotically flat spacetime, whereas particles with $E > 1$ can move to infinity, making limited orbits unobservable. At $E = 1$, particles can theoretically remain at rest at infinity. The energy $E = 1$ separates particles that are unable to move freely at infinity. It determines the existence of bounded orbits. The topological analysis indicates that the topological phase transition occurring at $E = 1$ effectively describes this physical feature.

Fig.3.9 (a) and 3.10 (b) display the results for Kerr BH with $M = 1$ and $a = 0.98$. These figures show the evolution of the TCO radius as a function of the control parameter for both prograde and retrograde scenarios. In retrograde cases, where $E < 0.96$, no TCO branches are present,resulting in a total topological number of zero. Two branches, one with a positive winding number and the other with a negative winding number, emerge from BP_1 at $E = 0.96$. A similar phenomenon is seen in the prograde near BP_2 at $E = 0.77$. Around the locations of BP_1 and BP_2, the following conditions hold

$$\frac{d^2E}{dr_t^2} = 0.7631 \ \ and \ \ 0.0018. \tag{3.81}$$

Thus, each of these bifurcation points can be considered a created point. The bifurcation points in Fig. 3.9 correspond to BP_1 and BP_2. Both positive winding number branches move towards infinity $r_t \to \infty$ as energy approaches one. As predicted, the total topological number remains constant at zero. When the energy exceeds one, there is only one branch for each clockwise direction, both having a winding number of $w = -1$. Consequently, the topological number W is -1 in these cases. These observations, with W transitioning from 0 to -1, highlight a topological phase transition occurring at $E = 1$. It is important to note that the winding number values are related to the TCO's stability. As demonstrated, TCOs with negative winding numbers are unstable; even minor disturbances can lead particles away from their orbits. Thus, only unstable TCOs exist for particles with $E > 1$. While the TCOs provide limited insight into astronomical visible effects, they help in understanding the overall structure of TCOs in BH environments.

Fig.3.9 (b) and 3.10 (b) illustrate the topological number W for prograde and retrograde scenarios, respectively. In all cases where $E < 1$, the topological number remains constant at zero, regardless of the presence of a bifurcation point. The topological number shifts to -1 when E exceeds 1, marking a topological phase transition at $E = 1$. In the preceding section, we particularly consider the value $a = 0.98$. It is important to examine whether the mass and spin of the BH influence the phase transition and topological structure. While variations in mass and spin affect the coefficients in vector expansions, they don't alter the asymptotic behaviours, as discussed in Section 3.4.2. As a result, the mass and spin of the BH don't affect the overall topological number. However, the positions of TCOs and MSCOs will change. The behaviour of ϕ^r at infinity determines the topological transition of phases at $E = 1$ and is constant for any mass or spin of the BH.

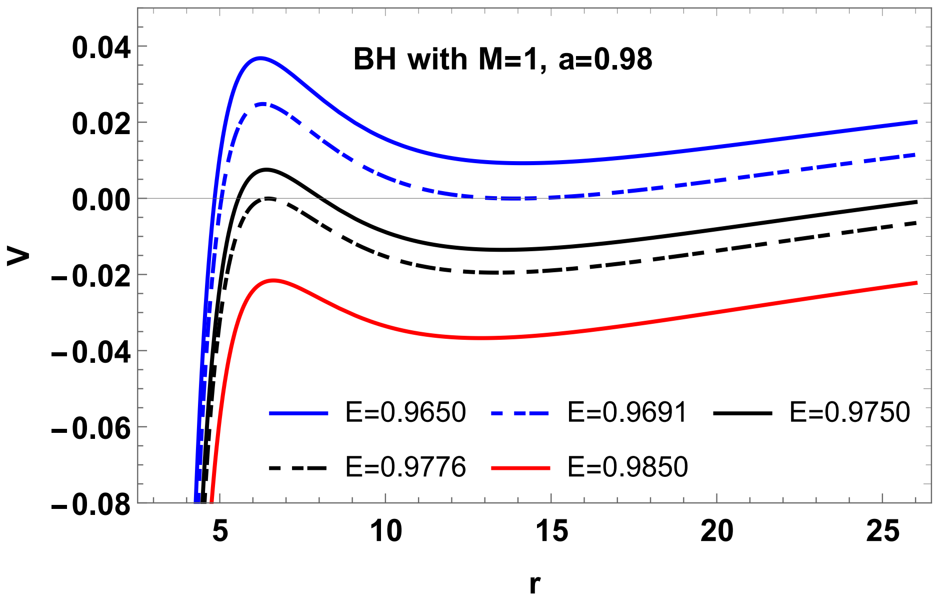

(a) $l = -4.5$

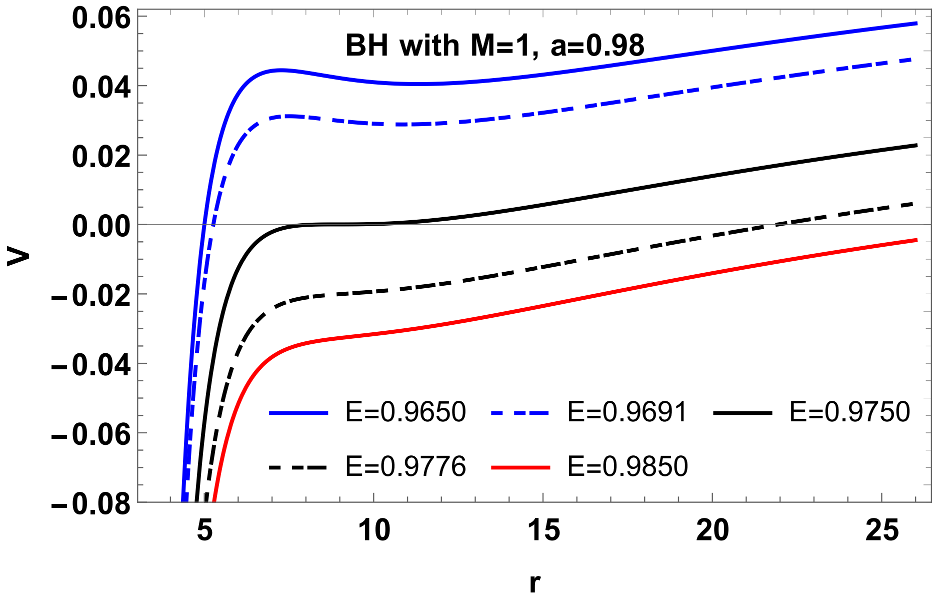

(b) $l = -4.2209$

Figure 3.4: The behaviour of the effective potential V with respect to r is plotted for BH $a = 0.98$, $M = 1$ and and various values of l and E. (a) The figure is potted for $l = -4.5$, and different values of $E = 0.9650$, 0.9691, 0.9750, 0.9850 which shows for these two particular values of E there are two TCOs whose radius are represented by black dots (their radii are approximately $r = 3.4666$ and $r = 7.7074$). (b) This figure is plotted for $l = -4.2209$, and different values of $E = 0.9450$, 0.9500, 0.9620, 0.9700, and 0.9800. It shows that for specific values of angular momentum, the two mentioned TCOs merge into a single orbit, known as the MSCO, with a radius represented by a black dot (approximately $r = 8.2027$).

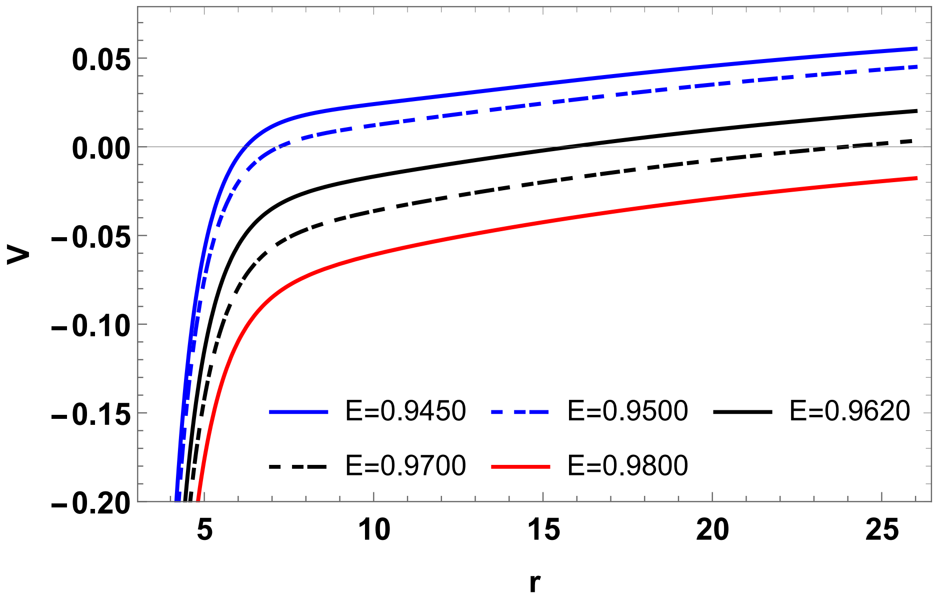

(a) $l = -4.0$

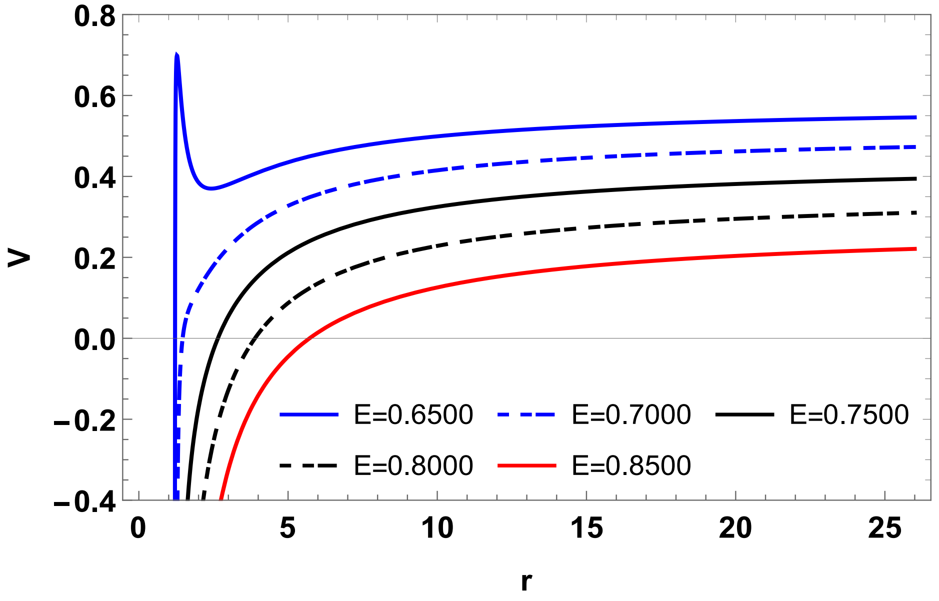

(b) $l = 1.5$

Figure 3.5: The behaviour of the effective potential V with respect to r is plotted for BH $a = 0.98$, $M = 1$, and various values of l and E. (a) The figure is potted for $l = -4.0$, and different values of $E = 0.9450$, 0.9500, 0.9620, 0.9700 and 0.9800. (b) This figure is plotted for $l = 1.5$, and different values of $E = 0.6500$, 0.7000, 0.7500, 0.8000, and 0.8500.

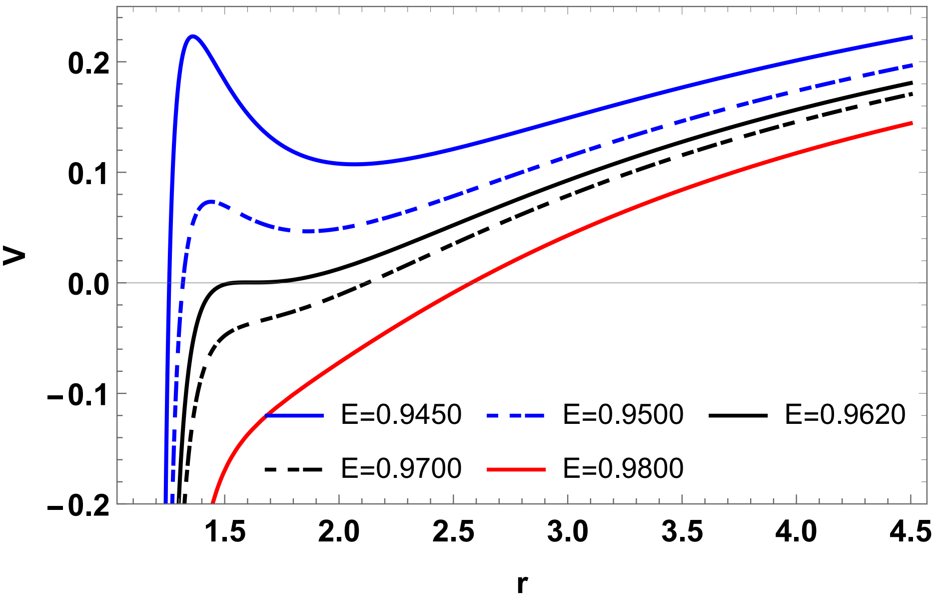

(a) $l = 1.6827$

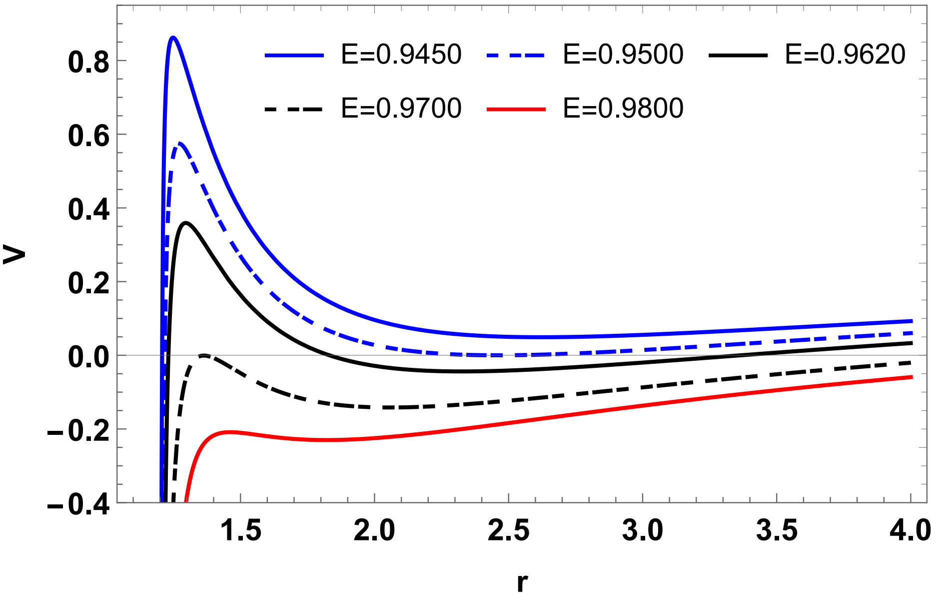

(b) $l = 1.9$

Figure 3.6: The behaviour of the effective potential V with respect to r is plotted for BH $a = 0.98$, $M = 1$, $\alpha = 0.8$ and and various values of l and E. (a) The figure is potted for $l = 1.6827$, and different values of $E = 0.7500$, 0.7600, 0.7661, 0.7700 and 0.7800 (b) This figure is plotted for $l = 1.9$, and different values of $E = 0..8100$, 0.8210, 0.8300, 0.8474, and 0.8600.

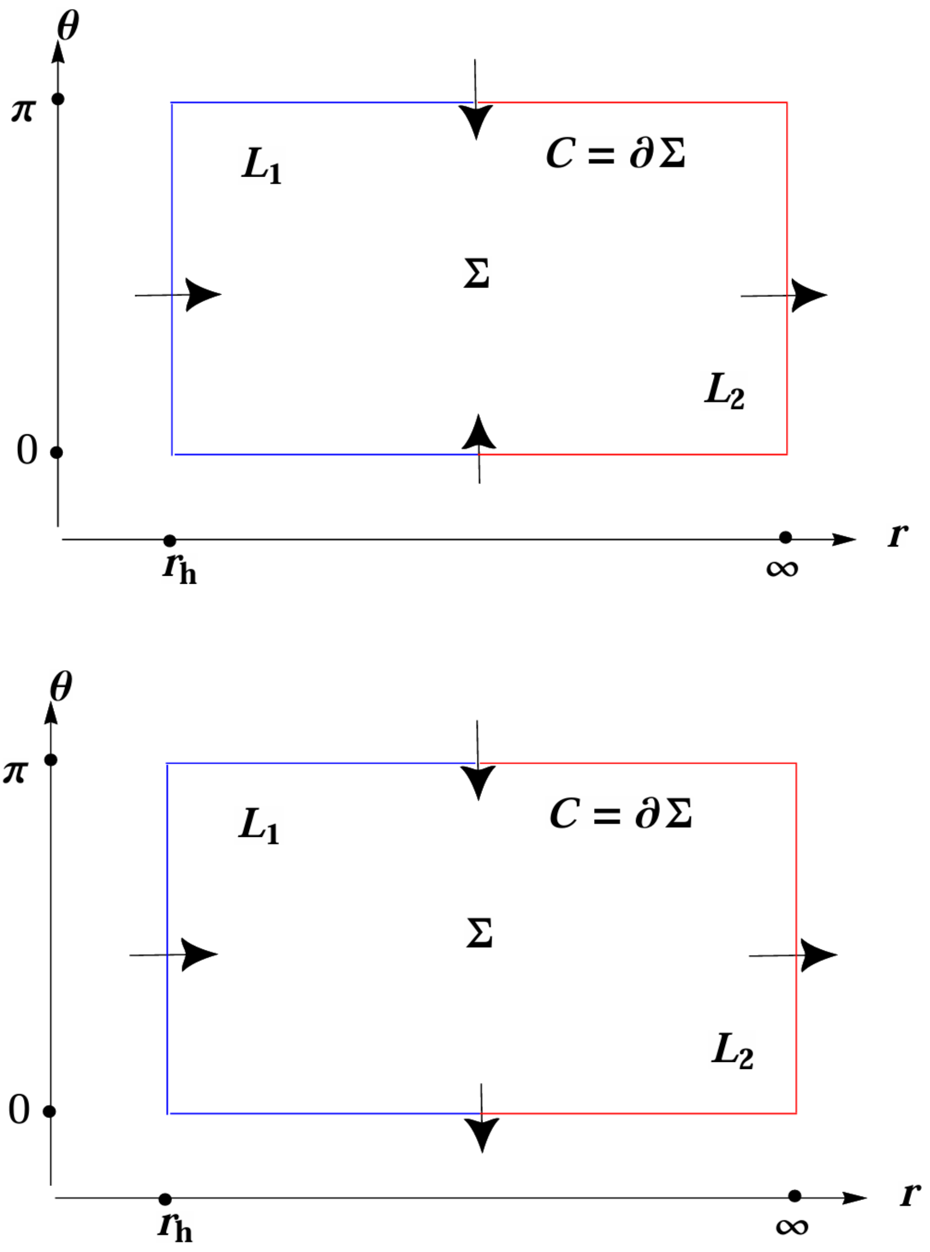

Figure 3.7: Changes in the direction of the vector ϕ at $\theta = 0$ and π.

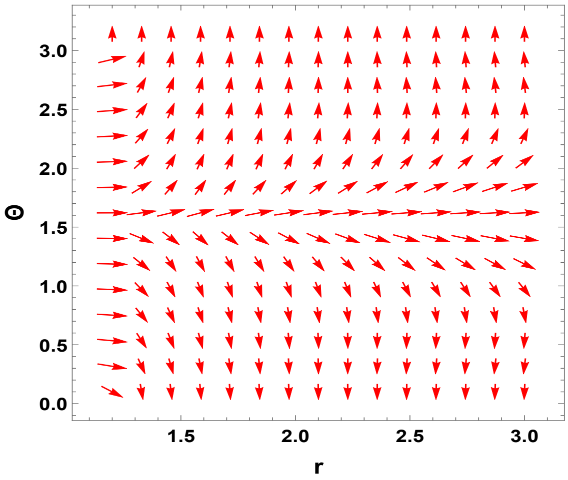

(a) $l = 1.5$

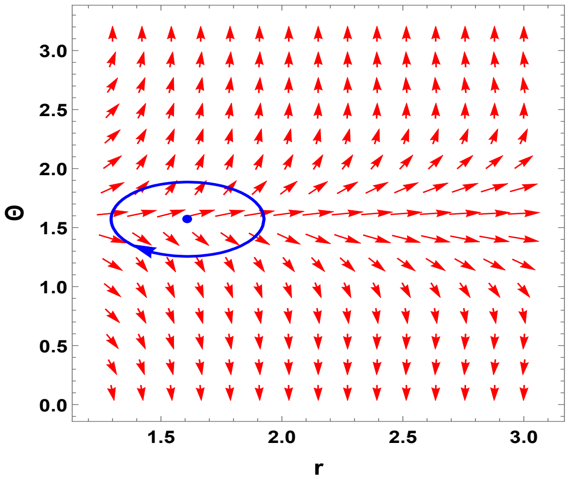

(b) $l = 1.6827$

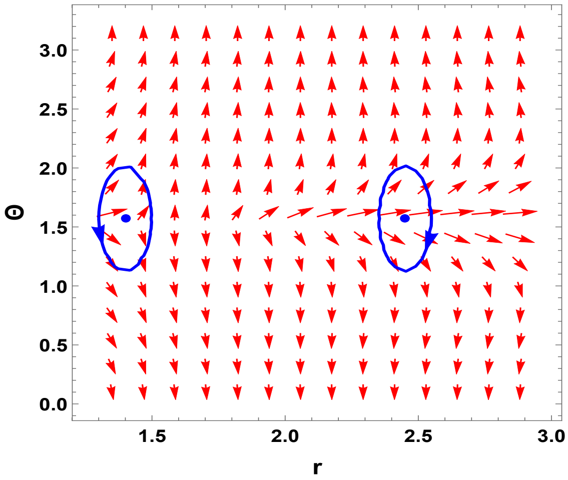

(c) $l = 1.90$

Figure 3.8: (a) The blue arrows represent the direction of unit vector n for $M = 1$, $a = 0.98$, and $l = 1.5$. (b) The red arrows represent the direction of the unit vector field n for $M = 1,\ a = 0.98,$ and $l = 1.9$.

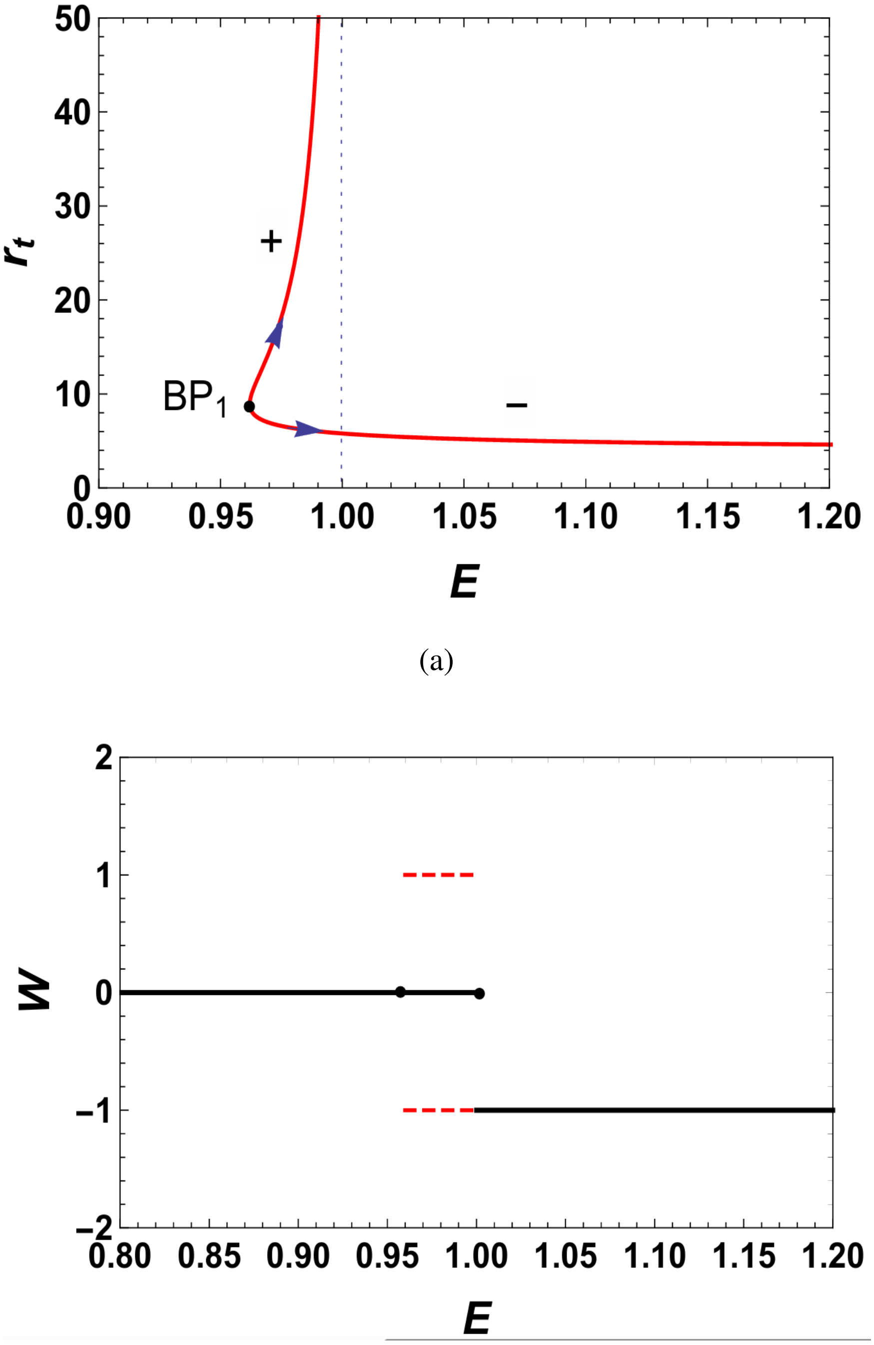

(a)

(b)

Figure 3.9: (a) The evolution of the radius r_t of the TCO is plotted against the energy E. The BP_1 represents the bifurcation point, where the upper branch, denoted by $+$, corresponds to a positive winding number, while the lower branch, denoted by $-$, corresponds to negative winding numbers. (b) This shows the topological number W relating to the TCOs as a function of E.

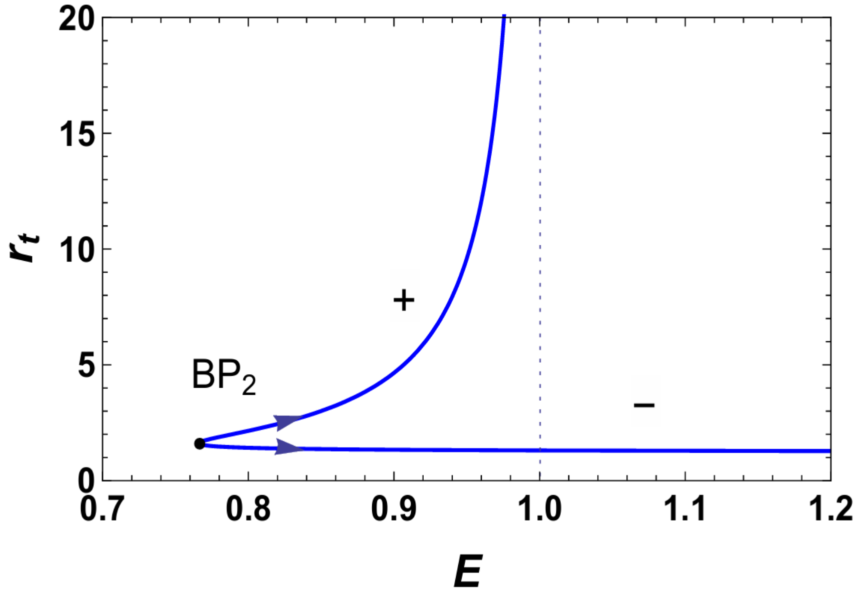

(a)

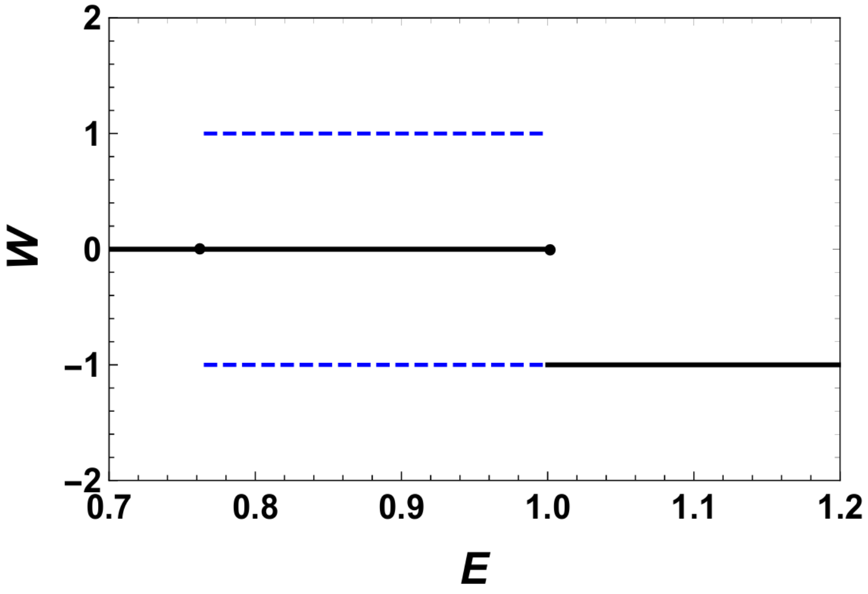

(b)

Figure 3.10: (a) The evolution of the radius r_t of the TCO is plotted against the energy E. The BP_2 represents the bifurcation point, where the upper branch, denoted by $+$, corresponds to a positive winding number, while the lower branch, denoted by $-$, corresponds to negative winding numbers. (b) This shows the topological number W relating to the TCOs as a function of E.

CHAPTER 4

TOPOLOGY OF TIMELIKE CIRCULAR ORBIT IN KERR-LIKE BLACK HOLE IN PERFECT FLUID DARK MATTER BACKGROUND

This chapter will discuss the topology of equatorial timelike circular orbits around a Kerr-like black hole in the perfect fluid dark matter (PFDM) background. Considering dark matter in black hole studies is crucial for a better understanding of the universe, as it is believed to play a critical role in galaxy formation and constitutes a significant portion of the universe. Therefore, examining the background is important for the topological study of circular orbits around black holes. The Kerr-like black hole in the PFDM background generalizes various black holes, and the results obtained can be reduced to previously known results.

4.1 Dark Matter

Dark matter is an elusive and mysterious component of the universe, remaining one of the most fascinating subjects in modern physics. Unlike conventional (visible) matter such as stars and planets [51], dark matter is difficult to detect because it does not emit, absorb, or reflect light or electromagnetic waves, making it invisible to current detection methods. Dark matter cannot simply be clouds of regular matter without stars, as this would result in detectable particles. It is not antimatter because it does not emit gamma rays in interactions with regular matter.

Additionally, unlike black holes, dark matter does not interact with its surroundings in ways that would be noticeable through small-scale phenomena.

Astrophysical observations have shown that dark matter is believed to make up about 27% of the universe's energy-mass content. Its gravitational effects are essential for understanding the formation and behaviour of galaxies, yet its true nature continues to puzzle scientists. Galaxies cannot exist in their current form without a significant portion of dark matter [52, 53]. This is because the gravitational attraction of visible matter is insufficient to keep stars tightly bound within galaxies. Without some form of invisible matter, stars would be more widely distributed throughout the galaxy. Dark matter is present both within and around us. Evidence for dark matter includes gravitational lensing and mass localization during galaxy collisions [54], as well as the large-scale structure of the universe [55]. Recent research has revealed that weakly interacting massive particles, are a leading candidate for dark matter [56]. Modifications to gravitational theories have been proposed. According to theoretical models and observations, the universe is composed of 68% dark energy, 27% dark matter, and 5% normal matter [51, 57].

4.2 Kerr-Like Black Holes in PFDM Background

The study of the BHs in the dark matter background environment is crucial, as dark matter is essential for the formation of most galaxies. The static BH in a PFDM background was studied by Li and Yang [58]. Their model is based on a single parameter, α, and matches a particular case first examined by Kiselev [59]. Specifically, they presented a logarithmic dependence to explain the asymptotic rotation curves for dark matter at great distances that is, in the halo-dominated region, in terms of the fundamental field. The lack of any proposed connection between dark matter and other fields, such as the dark energy field, could be a potential limitation of this model. A more comprehensive scenario, involving a mixture of more complex fields and additional dark matter properties, might be considered. A new Kerr BH solution incorporating dark matter effects has recently been published [58]. This solution requires modifications to the BHs ergosphere structure, among other things, as it alters the Kerr metric due to the presence of dark matter encoded by PFDM. Additionally, it allows for the investigation of the impact of PFDM on various astrophysical issues. The Kerr BH in a PFDM background has recently been used to study the black hole's emission rate [60], the shadow of the BH [61], and the detection angle.

The Kerr-like BH in a PFDM background has been studied in detail, including how it can be differentiated from a naked singularity in Ref. [62].

The line element of the Kerr-like BH in the PFDM background can be written as [50].

$$ds^2 = -\left(1-\frac{2Mr-\alpha r\ln\left(\frac{r}{\alpha}\right)}{\rho}\right)dt^2+\frac{\rho}{\Delta}dr^2-2a\sin^2\theta\left(\frac{2Mr-\alpha r\ln\left(\frac{r}{\alpha}\right)}{\rho}\right)dtd\phi$$
$$+\rho d\theta^2+\sin^2\theta\left(r^2+a^2+\sin^2\theta a^2\frac{2rM-\alpha r\ln\left(\frac{r}{\alpha}\right)}{\rho}\right)d\phi^2, \tag{4.1}$$

where

$$\Delta = r^2-2Mr+a^2+\alpha r\ln\left(\frac{r}{\alpha}\right), \tag{4.2}$$
$$\rho = r^2+a^2\cos^2\theta. \tag{4.3}$$

Here, α is the PFDM parameter, and a and M are the BH's mass and angular momentum per unit mass parameters. Note that, in the presence of PFDM and the additional parameter, α, in the horizon equation $\Delta = 0$, the location of the horizon differs from that of the Kerr BH. Thus, the black hole's size is affected by the PFDM parameter. However, PFDM does not change the number of horizons; like the Kerr black hole, the Kerr-like black hole in a PFDM background has two horizons: the inner horizon, r_-, and the outer (event) horizon, r_+. A detailed analysis of the horizons of the Kerr-like black hole in the PFDM background has been conducted in Ref [62]. The horizon equation can be solved to get the BH horizons;

$$\Delta = r^2-2Mr+a^2+\alpha r\ln\left(\frac{r}{|\alpha|}\right)=0. \tag{4.4}$$

It should be noted that there can be one, two, or no solutions to (4.4), depending on the parameters a and α chosen. The line element Eq. (4.1) in each example denotes NS, extremal BH, or BH with interior (r_-) and exterior (r_+) horizons, respectively. The PFDM stress-energy tensor $diag[-\rho, p_r, p_\theta, p_\phi]$ can be written as [50].

$$-\rho = p_r = \frac{r\alpha}{8\pi\rho^2}, \quad p_\theta = p_\phi = \frac{\alpha r}{8\pi\rho^2}\left(r-\frac{\rho}{2r}\right). \tag{4.5}$$

Using the Komar integrals the total BH mass M_T inside the surface of radius $r = r_0$, and the associated angular J_T around a rotational axis are given by [62].

$$M_T = M-\frac{\alpha\ln\left(\frac{r_0}{|\alpha|}\right)}{2ar_0}\left[ar_0+(r_0^2+a^2)\tan^{-1}\left(\frac{a}{r_0}\right)\right], \tag{4.6}$$

$$J_T = J+\frac{\alpha}{4a^2r_0}\left[(r_0^2+a^2)^2\tan^{-1}\left(\frac{a}{r_0}\right)-ar_0(r_0^2+a^2)-2a^3r_0\ln\left(\frac{r_0}{|\alpha|}\right)\right]. \tag{4.7}$$

4.3 Topology of Equatorial Timelike Circular Orbits Around Kerr-Like Black PFDM Background

To discuss, the topology for TCOs in Kerr-like BHs in PFDM we continue our discussion as in chapter 3. For that purpose, we define the n vector field and then discuss its asymptotic behaviour at the boundary and near the poles $\theta = 0, \pi$. To define the n vector field we use Eq. (3.34). The required quantity B for the topological analysis of TCOs in this case takes the form

$$B = \Delta \sin^2\theta, \tag{4.8}$$

The quantities $e_{1,2}$ [defined by Eq. (3.28)] required for n vector field for the Kerr-like black hole in PFDM backgrounds are obtained as

$$e_{1,2} = \frac{arl\left[2M - \alpha \ln\left(\frac{r}{\alpha}\right)\sin^2\theta\right] \pm \rho \csc\theta \sqrt{\Delta\left[l^2\rho^2 - a^2\Delta\sin^4\theta + (r^2+a^2)^2\sin^2\theta\right]}}{(a^2+r^2)^2 - a^2\Delta\sin^2\theta}, \tag{4.9}$$

In the equatorial plane, they are reduced to

$$e_{1,2} = \frac{2laMr \pm r\sqrt{\Delta\left((r^2+a^2)^2 + r^2l^2 - \Delta a^2\right)}}{(r^2+a^2)^2 - \Delta a^2}. \tag{4.10}$$

In Fig. (4.1) the effective potential for a BH with $a = 0.4$, $M = 1$, $\alpha = 0.8$ demonstrates its typical behaviour. Fig. 4.1 (a) is potted for $l = 2.0100$, and different values of $E = 1.0200$, 1.02105, 1.02150, 1.0220, and 1.0225 which shows for these two particular values of E there are two TCOs whose radius are represented by black dots (their radii are approximately $r = 3.4666$ and $r = 7.7074$). Fig. 4.1 (b) is plotted for $l = 2.0108$, and different values of $E = 1.0200$, 1.0210, 1.0215, 1.0220, and 1.0225. It can be seen that for specific values of angular momentum, the two mentioned timelike circular orbits merge into a single orbit, known as the MSCO, with a radius represented by a black dot (approximately $r = 8.2027$). There is one point with $E = 0.9691$, $E = 0.99776$, and $V = 0 = \partial_r V$ for every curve. These are the regions where the radial velocity of particles around the black hole is zero, indicating the presence of two TCOs for $l = 2.0100$. Fig. 4.1(b) shows that for a lower energy value and increased angular momentum ($l = 2.0108$), there are still two extremal points. As the energy increases, these points converge at a black dot with $E = 1.0210$, where $\partial_r V = 0$ is also satisfied. The dark dot, as expected, denotes the MSCO. It's worth noting, in particular, that such MSCO exactly fulfills the ISCO for the Kerr BHs. There will be no extreme point when the energy exceeds 0.9620. The effective potentials for $l = 2.0$ and $l = -2.0$ are illustrated in Figs. 4.2 (a) and 4.2(b). Although the angular momenta have different signs, the patterns remain similar. In both cases, no extremal points are observed regardless of energy variations, indicating the absence of TCOs. The effective potential is given in Fig. 4.3 (a) is plotted $a = 0.5$, $M = 1$ and $\alpha = 0.5$ for $l = -4.2$ and different values of E, $E = 0.92, 0.96, 1.00, 1.04$ and 1.08 similar pattern to that shown in Fig. 4.3 (b). is plotted for $l = 2.0$ and different values of $E = 0.94, 0.95, 0.96, 0.97$ and 0.98. The MSCO is given for particular a, l, and E values.

4.3.1 Vector and Asymptotic Behaviours

The aim is to analyze the asymptotic behaviour of the vector within the Kerr BH framework and check its consistency with the general scenario, which has been already described. While the vector can be derived using Eq. (3.34), this method is intricate and not elaborated upon here. As the vector approaches $\theta = 0$, we observe;

$$\phi^r = \frac{\partial_r e_1}{\sqrt{g_{rr}}}, \tag{4.11}$$

$$\begin{aligned}\phi^r(\theta \to 0) = &-\frac{l\left[(r+M)a^2 + (-3M+r)r^2 - \frac{\alpha}{2}\left\{r^2 + a^2 + \left(a^2 - 3r^2\right)\ln\left(\frac{r}{\alpha}\right)\right\}\right]}{(a^2+r^2)^{\frac{5}{2}}}\theta^{-1} \\ &+ \frac{a\sqrt{\Delta}l\left[2M\left(a^2 - 3r^2\right) - \alpha\left\{r^2 + a^2 + \left(a^2 - 3r^2\right)\ln\left(\frac{r}{\alpha}\right)\right\}\right]}{\left(a^2+r^2\right)^{7/2}} + O(\theta)^1.\end{aligned} \tag{4.12}$$

Similarly, the vector field component,

$$\phi^\theta = \frac{\partial_\theta e_1}{\sqrt{g_{\theta\theta}}}. \tag{4.13}$$

Near the axis $\theta = 0$,

$$\begin{aligned}\phi^\theta(\theta \to 0) = &\frac{-l\sqrt{\Delta}}{(a^2+r^2)^{\frac{3}{2}}}\theta^{-2} + \frac{\sqrt{\Delta}}{6l(r^2+a^2)^{\frac{7}{2}}}\Big[3a^6 + (-2l^2 + 9r^2)a^4 + ra^2\left\{9r^3 - (r+12M)l^2\right\} \\ &+ r^4(3r^2 + l^2) + 6a^2l^2r\alpha\ln\left(\frac{r}{\alpha}\right)\Big].\end{aligned} \tag{4.14}$$

Moreover, nearly $\theta = \pi$, we have;

$$\begin{aligned}\phi^r(\theta \to \pi) = &\,l\left[\frac{a^2(r+M) + (-3M+r)r^2 - \frac{\alpha}{2}\left\{r^2 + a^2 + \left(a^2 - 3r^2\right)\ln\left(\frac{r}{\alpha}\right)\right\}}{(r^2+a^2)^{\frac{5}{2}}}\right](\theta - \pi)^{-1} \\ &+ \frac{2a\sqrt{\Delta}Ml\left[a^2 - 3r^2 - \frac{\alpha}{2}\left\{r^2 + a^2 + \left(a^2 - 3r^2\right)\ln\left(\frac{r}{\alpha}\right)\right\}\right]}{(a^2+r^2)^{\frac{7}{2}}} + O(\theta - \pi),\end{aligned} \tag{4.15}$$

$$\begin{aligned}\phi^\theta(\theta \to \pi) = &\frac{l\sqrt{\Delta}}{(r^2+a^2)^{\frac{3}{2}}}(\theta - \pi)^{-2} - \frac{1}{6l(r^2+a^2)^{\frac{7}{2}}}\Big[\sqrt{\Delta}\Big\{3a^6 + (-2l^2 + 9r^2)a^4 \\ &+ a^2r\left\{9r^3 - l^2(r+12M)\right\} + \left(3r^2 + l^2\right)r^4 + 6a^2l^2r\ln\left(\frac{r}{\alpha}\right)\Big\}\Big].\end{aligned} \tag{4.16}$$

As a result, the vector's direction $arg\phi = arctan(\phi^{\theta}/\phi^{r})$ when $\theta = 0$ and $\theta = \pi$ is

$$arg\phi(\theta \to 0) \sim arctan\left(\frac{-l\sqrt{\Delta}}{(a^2+r^2)^{\frac{3}{2}}}\theta^{-2}\right) \sim arctan(-\theta^{-2}) = \frac{-\pi}{2}, \tag{4.17}$$

$$arg\phi(\theta \to \pi) \sim arctan\left(\frac{l\sqrt{\Delta}}{(a^2+r^2)^{\frac{3}{2}}}\theta^{-2}\right) \sim arctan(\theta^{-2}) = \frac{\pi}{2}. \tag{4.18}$$

Hence, the vector's positions are down at $\theta = 0$ and up at $\theta = \pi$. The vector can further be extended at large r on the equatorial plane, which provides

$$\phi^{r}(\theta = \frac{\pi}{2}, r \to \infty) = \frac{M}{r^2} - \frac{l^2}{r^3} + O\left(\frac{1}{r^4}\right). \tag{4.19}$$

The smallest positive parameter $\in = r - r_h$ is denoted near the horizon. The vector is then expanded near the horizon to give us

$$\phi^{r}(\theta = \frac{\pi}{2}, \in \to 0) = \frac{\sqrt{(-a^2+M^2)(l^2+M^2)}\left(M - \sqrt{a^2-M^2}\right)}{4a^2M^2} + O(\in^{\frac{1}{2}}). \tag{4.20}$$

The positive order of zero is significant. At the horizon and at large r, the vector's position aligns correctly since $\phi(\theta = \frac{\pi}{2}) = 0$. For $a = 0$, this results in

$$\phi^{r}(\theta = \frac{\pi}{2}, r \to r_{+}) = \frac{1}{4M}\sqrt{\frac{l^2}{4M^2} + 1}. \tag{4.21}$$

The Schwarzschild BH yields the exact result given in Eq. (3.41) with $\kappa = 1/4M$ and $g^{H}_{\phi\phi} = 4M^2$. In summary, the general formulation and the asymptotic behaviour of the vector in the Kerr BH scenario are consistent, indicating that the total topological number for TCOs in this context is zero.

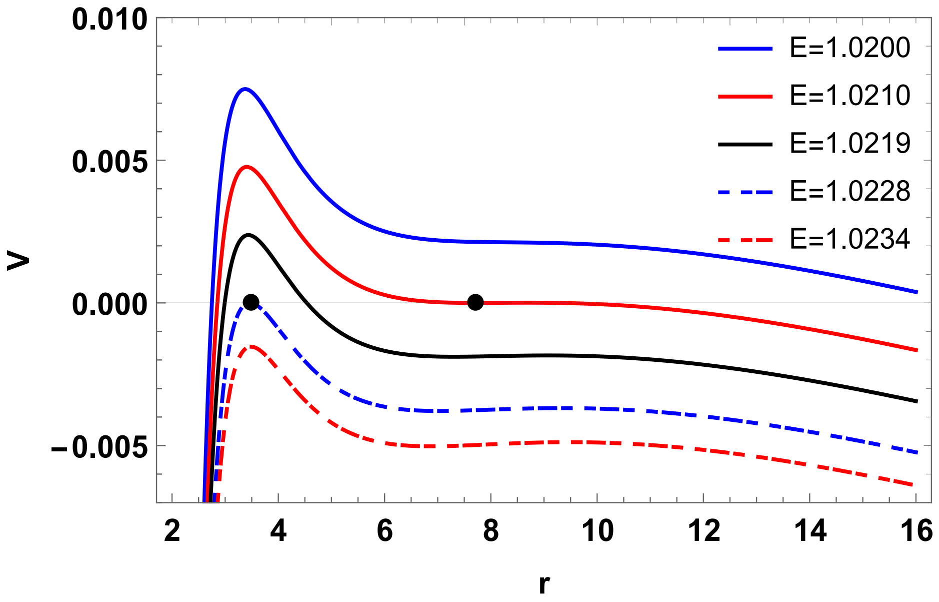

(a) $l = 2.0100$

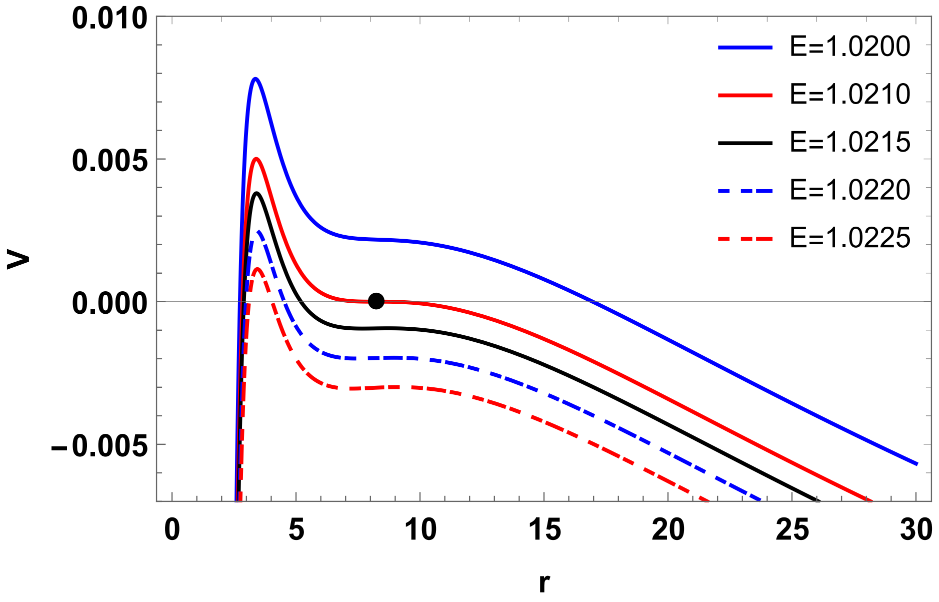

(b) $l = 2.0108$

Figure 4.1: The behaviour of the effective potential V with respect to r is plotted for BH $a = 0.4$, $M = 1$, $\alpha = 0.8$ and various values of l and E. (a) The figure is potted for $l = 2.0100$, and different values of $E = 1.0200$, 1.0210, 1.0219, 1.0228, and 1.0234 which shows for these two particular values of E there are two TCOs whose radius are represented by black dots (their radii are approximately $r = 3.4666$ and $r = 7.7074$). (b) This figure is plotted for $l = 2.0108$, and different values of $E = 1.0200$, 1.0210, 1.0215, 1.0220, and 1.0225. It shows that for specific values of $E = 1.0210$, the two mentioned TCOs merge into a single orbit, known as the MSCO, with a radius represented by a black dot (approximately $r = 8.2027$).

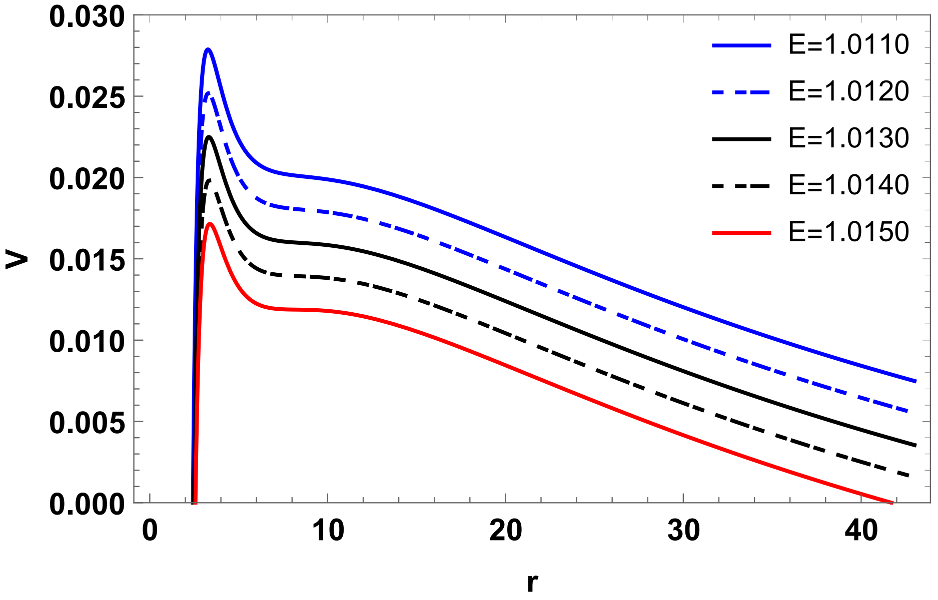

(a) $l = 2.0$

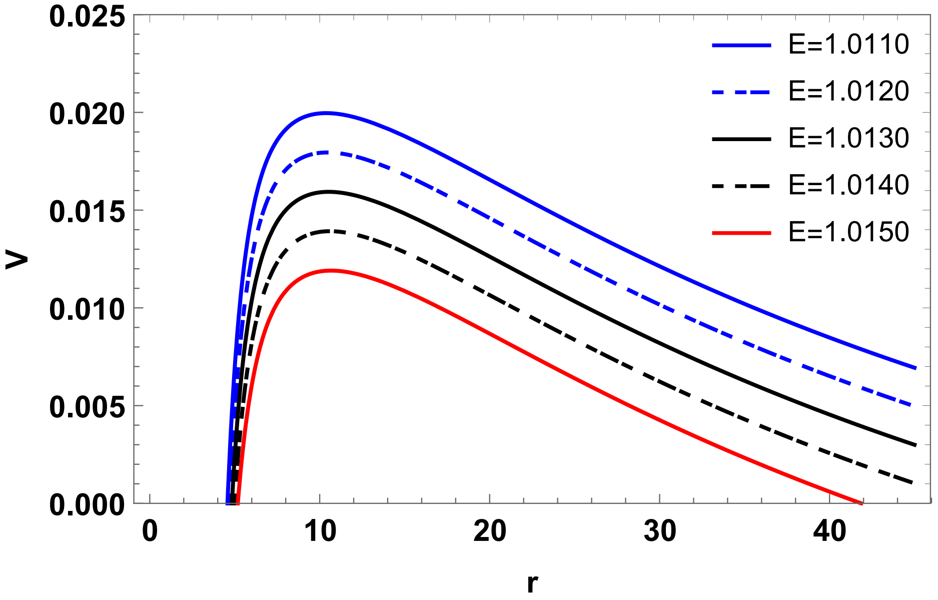

(b) $l = -2.0$

Figure 4.2: The behaviour of the effective potential V with respect to r is plotted for BH $a = 0.4$, $M = 1$, $\alpha = 0.8$ and various values of l and E. (a) The figure is potted for $l = 2.0$, and different values of $E = 1.0110$, 1.0120, 1.0130, 1.0140, and 1.0150. (b) This figure is plotted for $l = -2.0$, and different values of $E = 1.0110$, 1.0120, 1.0130, 1.0140, and 1.0150.

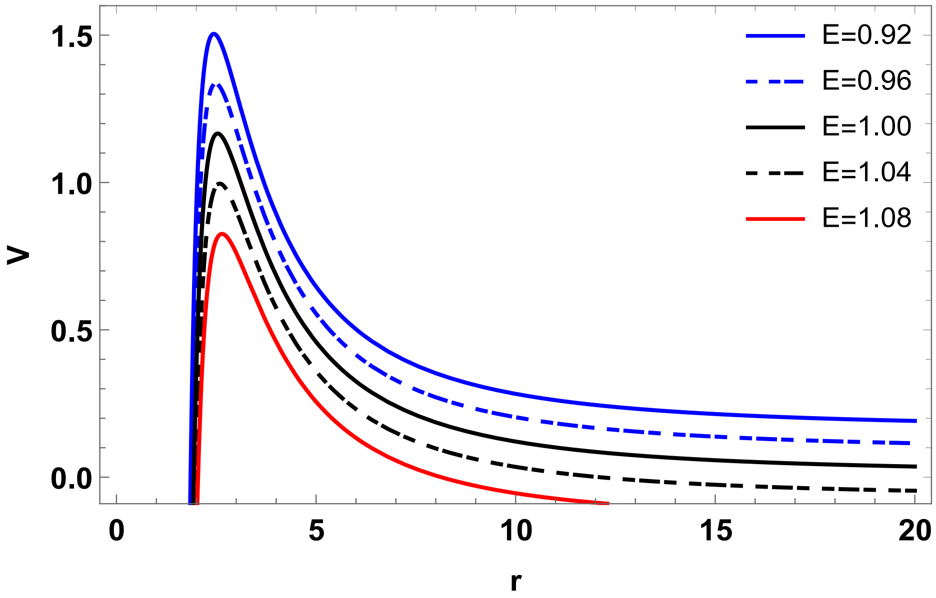

(a) $l = -4.2$

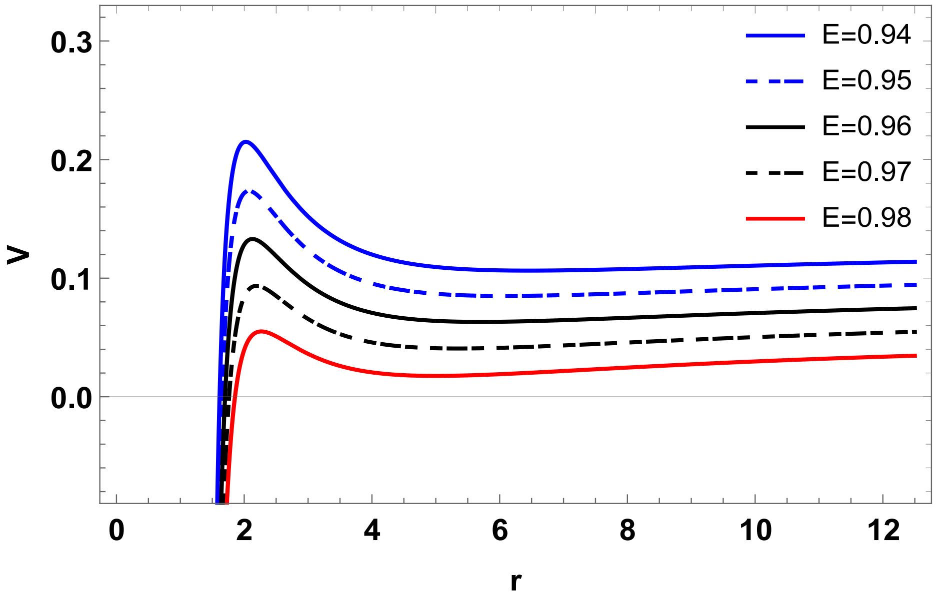

(b) $l = 2.0$

Figure 4.3: The behaviour of the effective potential V with respect to r is plotted for BH $a = 0.5$, $M = 1$, $\alpha = 0.5$ and various values of l and E. (a) The figure is potted for $l = -4.2$, and different values of $E = 0.92$, 0.96, 1.00, 1.04, and 1.08. (b) This figure is plotted for $l = 2.0$, and different values of $E = 0.94$, 0.95, 0.965, 0.97, and 0.98.

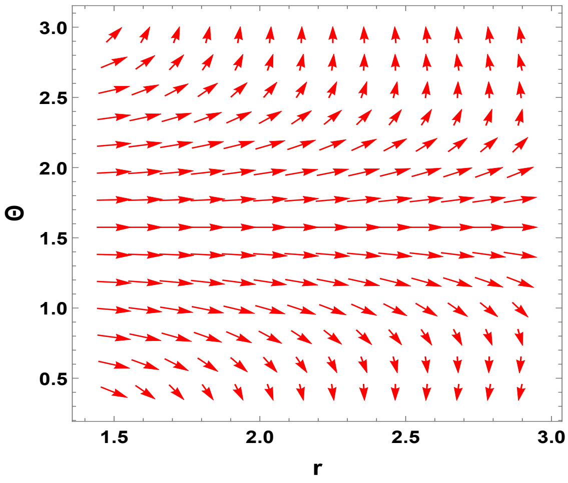

(a) $l = 1.5$

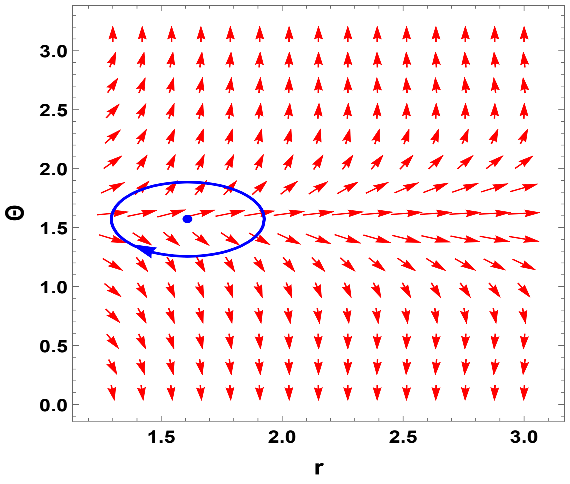

(b) $l = 1.6827$

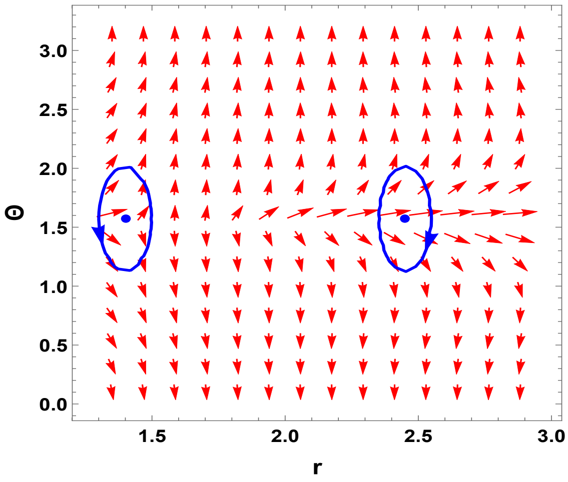

(c) $l = 1.90$

Figure 4.4: (a) The blue arrows represent the direction of unit vector n for $M = 1$, $a = 0.98$, and $l = 1.5$. (b) The red arrows represent the direction of the unit vector field n for $M = 1,\ a = 0.98,$ and $l = 1.9$.

CHAPTER 5

CONCLUSION

In this study, we built a strong framework for understanding the topology of trapped TCO within a general black hole spacetime, despite their close dependency on large particles' energy and angular momentum. Initially, we chose angular momentum as the control parameter. we started our analysis with timelike geodesics and used the effective potential to create a vector ϕ, similar to how we did with photons. The TCOs perfectly corresponded to the places where ϕ equals zero, allowing us to assign each TCO a local topological charge. we analyzed the behaviour of ϕ at the boundaries of the $r-\theta$ plane, focusing on the horizon, asymptotic limits, and the axis. we then explored the local and global topological characteristics of TCOs, discovering that unstable and stable TCO correspond to negative and positive winding numbers, respectively, from a local perspective. Specifically, TCOs either become unstable or vanish at the MSCO, which serves as a bifurcation point. The overall sum of the winding numbers remains constant before and after the bifurcation point. From a global perspective, we found that in a typical BH spacetime, the total topological number, which is calculated by summing the winding numbers of all 0 points, consistently equals zero. This indicates that stable and unstable TCOs with a given angular momentum always occur in pairs. Importantly, this finding is universal and unaffected by the particle's BHs or the angular momentum characteristics. However, it is crucial to note that in a typical BH scenario, the total topological number for LRs is -1, indicating the presence of a normal light ring LR. Specifically, in the case of a Kerr BH, the vector points to the right at $r=r_h$ and at infinity, and it points outward at $\theta=0$ and $\theta=\pi$. This continuous tendency shows that the Kerr BH has an overall topological number of TCOs $W=0$. As a result, unstable and stable TCOs typically appear in pairs when angular momentum l is used as the controlling parameter. Particularly, the MSCOs correspond to clockwise and counterclockwise rotations thus they act as bifurcation points. A created point corresponds to an MSCO with positive angular momentum, while a destroyed point corresponds to an MSCO with negative angular momentum. A created point corresponds to an MSCO with positive angular momentum, while a destroyed point corresponds to an MSCO with negative angular momentum. Although the potential of two or zero TCO branches for different angular momentum values, the total sum of the entire topological number is continuously 0, as predicted.

The test particle's energy is another control parameter in addition to angular momentum. As a result, we examine the topology for rotations that are both clockwise and counterclockwise. The results indicate that the total topological number is $W = 0$ for energies in the range $0 < E < 1$, and $W = -1$ for energies above $E = 1$. This suggests a topological phase transition at $E = 1$ in both prograde and retrograde scenarios, reflecting the independent motion of massive particles at infinity. Furthermore, in this case, the MSCOs exactly match to two produced locations. Before concluding this study, we would like to emphasize three distinctions in the topology of TCOs compared to LRs: (i) Unlike LRs, where energy and angular momentum are linearly related, TCOs have a nonlinear correlation between these quantities. (ii) The characteristics of the photon do not affect the radius of an LR while the black hole background remains constant, however, the test particle described has a significant impact on the radius of a TCO. This means that the circular orbit's degeneracy is interrupted by the existence of the mass in test particles, as shown in Fig. 3.10 (iii) In terms of total topological number, LRs have a value of $W = -1$, whereas TCOs have 0. This indicates that TCOs typically occur in pairs when angular momentum is held constant, and that standard LRs are found in at least one instance within a typical BH scenario. In this study, we have developed an extensive topological framework to analyze TCOs and applied this approach to the Kerr BH. We predict that by using this topological technique, we will obtain new insights on TCOs for both spinning and non-rotating black holes in general relativity or modified gravity theories. In addition, we plan to study more generic BH solutions that do not have Z_2 symmetry. The paper provides an in-depth examination of the topological characteristics of TCOs surrounding black holes, with a particular focus on the Kerr black hole. Using a topological approach, this study explores how the energy and angular momentum of test particles influence the behaviour and stability of TCOs. The findings reveal that TCOs always occur in pairs, consisting of one stable and one unstable orbit, with the total topological number remaining zero for a generic black hole. The paper also discusses the impact of black hole spin and test particle mass on the degeneracy of circular orbits. In addition, the paper explores the presence of closed timelike curves and the winding numbers that correspond with them, showing that TCOs always appear in pairs for a certain angular momentum. A critical energy value of $E = 1$ is identified as a key point for a topological phase transition, distinguishing between bounded and unbounded orbits. The results indicate that the topological approach effectively characterizes the physical features of test particle motion around a Kerr black hole. Furthermore, the paper explores the concept of TCOs, MSCOs, and ISCOs, analyzing their global and local behaviours and stability. The research provides illumination on black hole topological current objects within the (r, θ) plane, highlighting that TCOs always appear in pairs with a total sum of the topological number zero. The stability of TCOs is determined by the position of the vector ϕ, with positive winding numbers indicating stability.

In the Kerr BH background, the paper observes the presence of MSCOs that coincide with the ISCOs, displaying consistent stability and zero topological charges for TCOs. The topological charge of TCOs in the Kerr BH scenario is zero, as confirmed by the analysis of the effective potential and vector behaviour. Overall, the study provides a detailed and insightful examination of the topological properties of TCOs around black holes, offering valuable contributions to understanding test particle motion in these gravitational systems.

REFERENCES

[1] C. W. Misner, K. S. Thorne, J. A. Wheeler, and W. Gravitation, “Freeman and Company,” *San Francisco*, vol. 891, 1973.

[2] V. Frolov and I. Novikov, *Black Hole Physics: Basic Concepts and New Developments*. Springer Science & Business Media, 2012, vol. 96.

[3] E. Hubble, “A Relation Between Distance and Radial Velocity Among Extra-Galactic Nebulae,” *Proceedings of the National Academy of Sciences*, vol. 15, no. 3, pp. 168–173, 1929.

[4] Y. Wang and P. Mukherjee, “Observational Constraints on Dark Energy and Cosmic Curvature,” *Physical Review D*, vol. 76, no. 10, p. 103533, 2007.

[5] A. Qadir, *Einstein’s General Theory of Relativity*. Cambridge Scholars Publishing, 2020.

[6] J. Michell, “Vii. on the Means of Discovering the Distance, Magnitude, &c. of the Fixed Stars, in Consequence of the Diminution of the Velocity of their Light, in Case such a Diminution should be Found to Take Place in any of them, and such other data should be Procured from Observations, as would be Farther Necessary for that Purpose. by the rev. john michell, bdfrs in a letter to henry cavendish, esq. frs and as,” *Philosophical transactions of the Royal Society of London*, no. 74, pp. 35–57, 1784.

[7] C. Montgomery, W. Orchiston, and I. Whittingham, “Michell, Laplace and the Origin of the Black Hole Concept,” *Journal of Astronomical History and Heritage*, vol. 12, pp. 90–96, 2009.

[8] S. W. Hawking and G. F. Ellis, *The Large Scale Structure of Space-Time*. Cambridge University Press, 2023.

[9] E. M. Slayter and H. S. Slayter, *Light and Electron Microscopy*. Cambridge University Press, 1992.

[10] S. Chandrasekhar, “The Maximum Mass of Ideal White Dwarfs,” *Astrophysical Journal, vol. 74, p. 81*, vol. 74, p. 81, 1931.

[11] S.-W. Wei and Y.-X. Liu, “Topology of Equatorial Timelike Circular Orbits Around Stationary Black Holes,” *Physical Review D*, vol. 107, no. 6, p. 064006, 2023.

[12] J. R. Oppenheimer and G. M. Volkoff, “On Massive Neutron Cores,” *Physical Review*, vol. 55, no. 4, p. 374, 1939.

[13] A. Einstein, “On a Stationary System with Spherical Symmetry Consisting of many Gravitating Masses,” *Annals of Mathematics*, pp. 922–936, 1939.

[14] J. R. Oppenheimer and H. Snyder, “On Continued Gravitational Contraction,” *Physical Review*, vol. 56, no. 5, p. 455, 1939.

[15] E. Salpeter, “Accretion of Interstellar Matter by Massive Objects,” *Publications*, vol. 1, p. 165, 1964.

[16] Y. Zel’dovich, “The Fate of a Star and the Evolution of Gravitational Energy upon Accretion,” *Neutron Stars, Black Holes, and Binary X-Ray Sources*, vol. 48, p. 329, 1975.

[17] S. Bowyer, E. Byram, T. Chubb, and H. Friedman, “Cosmic X-ray Sources,” *Science*, vol. 147, no. 3656, pp. 394–398, 1965.

[18] B. P. Abbott, R. Abbott, T. Abbott, M. Abernathy, F. Acernese, K. Ackley, C. Adams, T. Adams, P. Addesso, R. X. Adhikari *et al.*, “Observation of Gravitational Waves from a Binary Black Hole Merger,” *Physical review letters*, vol. 116, no. 6, p. 061102, 2016.

[19] B. P. Abbott, R. Abbott, T. Abbott, M. Abernathy, F. Acernese, K. Ackley, C. Adams, T. Adams, P. Addesso, R. Adhikari *et al.*, “Gw151226: observation of Gravitational Waves from a 22-Solar-Mass Binary Black Hole Coalescence,” *Physical review letters*, vol. 116, no. 24, p. 241103, 2016.

[20] E. H. TelescopeCollaboration, R. Azulay, A.-K. Baczko, S. Britzen, G. Desvignes, R. Eatough, R. Karuppusamy, J.-Y. Kim, M. Kramer, T. Krichbaum *et al.*, “First M87 Event Horizon Telescope Results. ii. Array and Instrumentation,” *apjl*, vol. 875, no. 1, p. L2, 2019.

[21] R. E. Langer and G. D. Birkhoff, *Relativity and Modern Physics, by George David Birkhoff with the Cooperation of Rudolph Ernest Langer*. Harvard University pres, 1923.

[22] S.-W. Wei, Y.-P. Zhang, Y.-X. Liu, and R. B. Mann, “Static Spheres Around Spherically Symmetric Black Hole Spacetime,” *Physical Review Research*, vol. 5, no. 4, p. 043050, 2023.

[23] S. Hawking, *A Brief History of Time: from Bbig Bang to Black Holes*. Random House, 2009.

[24] B. Schutz, *A First Course in General Relativity*. Cambridge University Press, 2022.

[25] I. Misner and T. CW, “Ks and Wheeler, Ja (1973). Gravitation.”

[26] A. Potts, *The Science/Fiction of sex: Feminist Deconstruction and the Vocabularies of Heterosex*. Routledge, 2014.

[27] E. H. T. Collaboration *et al.*, “First m87 Eevent Horizon Telescope Results. iv. Imaging the Central Supermassive Black Hole,” *arXiv preprint arXiv:1906.11241*, 2019.

[28] M. Dvornikov, “Gravitational Scattering of Spinning Neutrinos by a Rotating Black Hole with a Slim Magnetized Accretion Disk,” *Classical and Quantum Gravity*, vol. 40, no. 1, p. 015002, 2022.

[29] P. V. Cunha and C. A. Herdeiro, “Stationary Black Holes and Light uppercaseRings,” *Physical Review Letters*, vol. 124, no. 18, p. 181101, 2020.

[30] A. Das, A. Saha, and S. Gangopadhyay, “Investigation of Circular Geodesics in a Rotating Charged Black uppercaseHole in the Presence of Perfect Fluid Dark Matter,” *Classical and Quantum Gravity*, vol. 38, no. 6, p. 065015, 2021.

[31] M. Guo and S. Gao, “Universal Properties of Light Rings for Stationary Axisymmetric Spacetimes,” *Physical Review D*, vol. 103, no. 10, p. 104031, 2021.

[32] H. C. L. Junior, P. V. Cunha, C. A. Herdeiro, and L. C. Crispino, “Shadows and Lensing of Black Holes Immersed in Strong Magnetic Fields,” *Physical Review D*, vol. 104, no. 4, p. 044018, 2021.

[33] H.-S. Liu, Z.-F. Mai, Y.-Z. Li, and H. Lü, “Quasi-Topological Electromagnetism: Dark Energy, Dyonic Bblack Holes, Stable Photon Spheres and Hidden Electromagnetic Duality,” *Science China Physics, Mechanics & Astronomy*, vol. 63, pp. 1–15, 2020.

[34] R. Ghosh and S. Sarkar, “Light Rings of Stationary Spacetimes,” *Physical Review D*, vol. 104, no. 4, p. 044019, 2021.

[35] S.-W. Wei, “Topological Charge and Bblack Hhole Photon Spheres,” *Physical Review D*, vol. 102, no. 6, p. 064039, 2020.

[36] P. V. Cunha, E. Berti, and C. A. Herdeiro, “Light-ring Stability for Ultracompact Objects,” *Physical review letters*, vol. 119, no. 25, p. 251102, 2017.

[37] M. Rizwan and K. Jusufi, “Topological Classes of Thermodynamics of Black Holes in Perfect Fluid Dark Matter Background,” *The European Physical Journal C*, vol. 83, no. 10, p. 944, 2023.

[38] V. Cardoso, L. C. Crispino, C. F. Macedo, H. Okawa, and P. Pani, “Light Rings as Observational Evidence for Event Horizons: Long-lived Modes, Ergoregions and Nonlinear Instabilities of Ultracompact Objects,” *Physical Review D*, vol. 90, no. 4, p. 044069, 2014.

[39] S. Hod, “On the Number of Light Rings in Curved Spacetimes of Ultra-compact Objects,” *Physics Letters B*, vol. 776, pp. 1–4, 2018.

[40] H. C. L. Junior, J.-Z. Yang, L. C. Crispino, P. V. Cunha, and C. A. Herdeiro, “Einstein-maxwell-dilaton Neutral Black Holes in Strong Magnetic Fields: Topological Charge, Shadows, and Lensing,” *Physical Review D*, vol. 105, no. 6, p. 064070, 2022.

[41] S.-W. Wei, Y.-X. Liu, and R. B. Mann, “Black Hole Solutions as Topological Thermodynamic Defects,” *Physical Review Letters*, vol. 129, no. 19, p. 191101, 2022.

[42] P. Cunha, J. Grover, C. Herdeiro, E. Radu, H. Runarsson, and A. Wittig, “Chaotic Lensing Around Boson Stars and Kerr Black Holes with Scalar Hair,” *Physical Review D*, vol. 94, no. 10, p. 104023, 2016.

[43] P. V. Cunha, C. A. Herdeiro, and E. Radu, “Fundamental Photon Orbits: Black Hole Shadows and Spacetime Instabilities,” *Physical Review D*, vol. 96, no. 2, p. 024039, 2017.

[44] Y. Duan, “The Structure of the Topological Current,” *Preprint SLAC-PUB-3301/84*, 1984.

[45] J. Carot, "Some Developments on Axial Symmetry," *Classical and Quantum Gravity*, vol. 17, no. 14, p. 2675, 2000.

[46] J. F. Delgado, C. A. Herdeiro, and E. Radu, "Equatorial Timelike Circular Orbits Aaround Eneric ultracompact Objects," *Physical Review D*, vol. 105, no. 6, p. 064026, 2022.

[47] C. A. Herdeiro and E. Radu, "Kerr Black uppercaseHoles with Scalar Hair," *Physical review letters*, vol. 112, no. 22, p. 221101, 2014.

[48] J. F. Delgado, C. A. Herdeiro, and E. Radu, "Rotating Axion Boson Stars," *Journal of Cosmology and Astroparticle Physics*, vol. 2020, no. 06, p. 037, 2020.

[49] L.-B. Fu, Y.-S. Duan, and H. Zhang, "Evolution of the Chern-simons Vortices," *Physical Review D*, vol. 61, no. 4, p. 045004, 2000.

[50] Z. Xu, X. Hou, and J. Wang, "Kerr–anti-de Sitter/de Sitter Black Hole in Perfect Fluid Dark Matter Background," *Classical and Quantum Gravity*, vol. 35, no. 11, p. 115003, 2018.

[51] P. A. Ade, N. Aghanim, M. Alves, C. Armitage-Caplan, M. Arnaud, M. Ashdown, F. Atrio-Barandela, J. Aumont, H. Aussel, C. Baccigalupi *et al.*, "Planck 2013 Results. i. Overview of Products and Scientific Results," *Astronomy & Astrophysics*, vol. 571, p. A1, 2014.

[52] J. H. Oort, "The Force Exerted by the Stellar System in the Direction Perpendicular to the Galactic Plane and Some Related Problems," *Bulletin of the Astronomical Institutes of the Netherlands, Vol. 6, p. 249*, vol. 6, p. 249, 1932.

[53] S. M. Faber and J. Gallagher, "Masses and Mass-to-Light Ratios of Galaxies," *Annual review of astronomy and astrophysics*, vol. 17, no. 1, pp. 135–187, 1979.

[54] D. Clowe, M. Bradač, A. H. Gonzalez, M. Markevitch, S. W. Randall, C. Jones, and D. Zaritsky, "A Direct Empirical Proof of the Existence of Dark Matter," *The Astrophysical Journal*, vol. 648, no. 2, p. L109, 2006.

[55] P. J. E. Peebles, *The Llarge-Scale Structure of the Universe*. Princeton University Press, 1980, vol. 12.

[56] C. J. Copi, D. N. Schramm, and M. S. Turner, "Big-bang Nucleosynthesis and the Baryon Density of the Universe," *Science*, vol. 267, no. 5195, pp. 192–199, 1995.

[57] L. Amendola and S. Tsujikawa, *Dark Eenergy: Theory and Observations*. Cambridge University Press, 2010.

[58] M.-H. Li and K.-C. Yang, “Galactic Dark Matter in the Phantom Field,” *Physical Review D—Particles, Fields, Gravitation, and Cosmology*, vol. 86, no. 12, p. 123015, 2012.

[59] V. Kiselev, “Quintessence and Black Holes,” *Classical and Quantum Gravity*, vol. 20, no. 6, p. 1187, 2003.

[60] X. Hou, Z. Xu, and J. Wang, “Rotating Bblack Hole Shadow in Perfect Fluid Dark Matter,” *Journal of Cosmology and Astroparticle Physics*, vol. 2018, no. 12, p. 040, 2018.

[61] S. Haroon, M. Jamil, K. Jusufi, K. Lin, and R. B. Mann, “Shadow and Deflection Angle of Rotating Black Holes in Perfect Fluid Dark Matter with a Cosmological Constant,” *Physical Review D*, vol. 99, no. 4, p. 044015, 2019.

[62] M. Rizwan, M. Jamil, and K. Jusufi, “Distinguishing a Kerr-Like Black Hole and a Naked Singularity in Perfect Fluid Dark Matter Via Precession Frequencies,” *Physical Review D*, vol. 99, no. 2, p. 024050, 2019.